The Astrophysical Journal, 961:239 (17pp), 2024 February 1 https://doi.org/10.3847/1538-4357/ad036e

Probing the Subparsec Dust of a Supermassive Black Hole with the Tidal Disruption Event AT 2020mot

Megan Newsome[1,2], Iair Arcavi[3,4], D. Andrew Howell[1,2], Jamison Burke[1,2], Kishalay De[5,8], Yael Dgany[3],
Sara Faris[3], Joseph Farah[1,2], Daichi Hiramatsu[6,7], Curtis McCully[1], Estefania Padilla-Gonzalez[1,2],
Craig Pellegrino[1,2], and Giacomo Terreran[1]
[1] Las Cumbres Observatory, 6740 Cortona Drive, Suite 102, Goleta, CA 93117-5575, USA
[2] Department of Physics, University of California, Santa Barbara, CA 93106-9530, USA
[3] School of Physics and Astronomy, Tel Aviv University, Tel Aviv 69978, Israel
[4] CIFAR Azrieli Global Scholars program, CIFAR, Toronto, Canada
[5] MIT-Kavli Institute for Astrophysics and Space Research, 77 Massachusetts Ave., Cambridge, MA 02139, USA
[6] Center for Astrophysics | Harvard & Smithsonian, 60 Garden Street, Cambridge, MA 02138-1516, USA
[7] The NSF AI Institute for Artificial Intelligence and Fundamental Interactions, USA

Received 2023 May 3; revised 2023 October 11; accepted 2023 October 12; published 2024 January 30

Abstract

AT 2020mot is a typical UV/optical tidal disruption event (TDE) with no radio or X-ray signatures in a quiescent host. We find an *i*-band excess and rebrightening along the decline of the light curve which could be due to two consecutive dust echoes from the TDE. We model our observations following van Velzen et al. and find that the near-infrared light curve can be explained by concentric rings of thin dust within ∼0.1 pc of a $\sim 6 \times 10^6\ M_\odot$ supermassive black hole (SMBH), among the smallest scales at which dust has been inferred near SMBHs. We find dust covering factors of order $f_c \leqslant 2\%$, much lower than found for dusty tori of active galactic nuclei. These results highlight the potential of TDEs for uncovering the environments around black holes when including near-infrared observations in high-cadence transient studies.

Unified Astronomy Thesaurus concepts: Tidal disruption (1696); Ultraviolet transient sources (1854); Astrophysical dust processes (99)

1. Introduction

Tidal disruption events (TDEs) occur when a star's self-gravity is disturbed by the tidal forces of a supermassive black hole (SMBH), after which the infall of the stripped, stellar debris causes a bright flare that can be observed in the optical and X-ray regimes (Rees 1988; Evans & Kochanek 1989; Komossa & Bade 1999). The evolution of TDE light curves will vary based on the SMBH's mass, the unlucky star's mass before its tidal unraveling, and the depth of the impact. Furthermore, the source of the UV/optical emission is debated, whether as a result of the debris producing stream shocks on its fallback journey toward the SMBH (Piran et al. 2015), or if the material has already completed that journey and the flare is a result of accretion emission being reprocessed into the optical regime (Guillochon et al. 2014; Jiang et al. 2016b; Roth et al. 2016). Therefore TDE observations are often heralded as windows into accretion mechanisms, jet formation, and feedback effects on local and large-scale galactic environments. However, these implications are not yet well explored. In just a decade, the number of observed TDEs has escalated quickly with over 50 reported to the Transient Name Server[9] in the last 5 yr, and this increase in discoveries allows for large-sample statistics on TDE rates and host galaxy dependencies (e.g., Graham et al. 2019; van Velzen et al. 2021a; Hammerstein et al. 2023; Yao et al. 2023). We can now single out exceptional observations that probe the physics of accretion and feedback on subparsec scales around quiescent galactic nuclei.

If the tidal disruption flare interacts with circumnuclear dust, the effect can be observed as time-dependent reddening that allows deduction of the dust's geometry and location, and such visible signatures may be concurrent with the initial flare. Interaction with dust, for example, can cause a "dust echo" in which the dust is heated from the incident light and subsequently reemits in the infrared (IR). Reprocessing light curves have long been used as probes of dust in other energetic phenomena like active galactic nuclei (AGN; e.g., Barvainis 1987) and supernovae (e.g., Dwek 1983; Patat 2005). The time delay at which a reprocessed IR light curve becomes visible depends on how close the dust is to the central flare, while the shape of the reprocessed light curve varies with the dust's geometry. TDEs offer the unique chance to reveal dust at subparsec scales to quiescent SMBHs.

Just over a dozen dust echoes have been reported for candidate TDEs (e.g., Jiang et al. 2016a, 2017, 2021; Dou et al. 2016; van Velzen et al. 2016; Li et al. 2020; Stein et al. 2021; Onori et al. 2022; Wang et al. 2022), using mid-infrared (MIR) data from the AllWISE and NEOWISE releases of the Wide-field Infrared Survey Explorer (WISE; Wright et al. 2010; Mainzer et al. 2014), most finding 2–5 epochs of MIR brightening after optical discovery of each TDE between 100 and 200 days after optical peak (van Velzen et al. 2021a). Only eight of these events are in quiescent galaxies, seven of which have accompanying X-ray data alongside UV/optical detections (van Velzen et al. 2021a; Jiang et al. 2021). Two of these, ASASSN-14li and AT 2019dsg, were detected in the radio as well (Jiang et al. 2016b; Stein et al. 2021). Using the delay between the UV/optical peak and rebrightening in MIR, the distance between the flare and the nearby dust was found to be

---

[8] NASA Einstein Fellow.

[9] https://www.wis-tns.org/

∼0.1–0.8 pc for the eight events, and these echoes in quiescent galaxies subsequently show dust covering factors (fraction of the accretion disk or SMBH environment that is obscured by dust) of $f_c \sim 0.01$, notably lower than $f_c \sim 0.2$–0.5 as found in AGN (Jiang et al. 2019; van Velzen et al. 2021a).

AT 2020mot was discovered by the Zwicky Transient Facility (ZTF) on MJD 59,014.39 (2020 June 14) as a nuclear transient (Forster et al. 2020), later classified by the Global Supernova Project as a TDE (Hosseinzadeh et al. 2020) given its central location to the host galaxy at (R.A., decl.) = (00:31:13.57, +85:00:31.9) and broad He II emission feature. Hammerstein et al. (2023) include AT 2020mot in their sample of 30 TDEs, classifying it as a "TDE-H+He" from observed broad Hα and He II. Liodakis et al. (2023) also report polarized emission from AT 2020mot that is the highest measured for a TDE without a jet, with radio upper limits of 27 μJy at 15 GHz.

Here we present data from Las Cumbres Observatory which reveal that AT 2020mot was still emitting significant light in the *i* band as of +800 days from optical peak. We explain this IR excess in an otherwise normal TDE as the result of a dust echo, in which dust near the SMBH is physically thin and close enough to respond promptly (within months) to the flare, heating up and reemitting light in the near-infrared (NIR).

2. Observations and Data Processing

Throughout this work, we use observations taken by Las Cumbres Observatory, ZTF (Bellm et al. 2019), the Niel Gehrels Swift Observatory (Swift; Gehrels et al. 2004), and WISE (Wright et al. 2010). All phases are expressed in the observer frame throughout this work.

2.1. Optical Photometry and Spectroscopy

We obtained *BgVri*-band images with the Sinistro cameras on Las Cumbres' 1.0 m telescopes, performed image subtraction, and extracted point-spread function (PSF) photometry with the `lcogtsnpipe` pipeline[10] (Valenti et al. 2016). *BV*-band photometry was calibrated to Vega magnitudes and *gri*-band photometry was calibrated to the AB magnitude system. Zero-points for all bands were calculated from the magnitudes of field stars as listed in the AAVSO Photometry All-Sky Survey (Henden et al. 2009).

Host subtraction isolates the evolution of the flare alone without contamination from the host galaxy. Upon subtraction of the science images with Las Cumbres images taken at +490 days from *g*-band peak, comparison to the ZTF forced photometry in the *gr* bands at the same epochs, the Las Cumbres subtracted images showed a subtle but clear oversubtraction, indicating residual TDE light. We thus adjusted `lcogtsnpipe` to use archival images (MJDs 55,914.0 in *g* band, 55,957.0 in *r* band, and 55,991.0 in *i* band) from the Panoramic Survey Telescope and Rapid Response System (Pan-STARRS1 or PS1; Kaiser et al. 2010) as templates for image subtraction in the *gri* bands. We have since acquired several epochs of Las Cumbres data intended for use as templates, most recently at +800 days from *g*-band peak, all of which show residual TDE flux in the *i* band when subtracted with PS1 templates, while the *gr* bands had entirely faded beyond Las Cumbres's detection thresholds and showed no residual flux from PS1 subtractions. Indeed, using the +800 day images as subtraction templates produce a light curve that is 0.3 mag fainter in *i* band compared to equivalent subtractions with PS1 templates. We therefore find that the TDE was still emitting light above the baseline host level in the *i* band at the end of 2022, and use PS1 templates to subtract all *gri*-band data uniformly. We note that subtracting the *gr*-band data with both Las Cumbres and PS1 templates gives the same results, affirming the reliability of the PS1 subtractions.

For the *BV* bands, the +800 day images from Las Cumbres were used as templates. All subtraction was performed using the HOTPANTS[11] image subtraction algorithm (Alard & Lupton 1998; Becker 2015), with normalization to the science image and convolution to the template image.

Supplemental photometry in the *gr* bands was obtained from the ZTF forced photometry server[12] (Masci et al. 2019). These data cover the first detection at MJD = 59,014.39 and the subsequent rise to peak, while the Las Cumbres data begin near *g*-band peak at MJD = 59,078.38. We visually checked the ZTF difference images for nondetections and otherwise excluded data with magnitude errors greater than 0.1.

We have also corrected all photometry for Galactic extinction with $A_V = 0.238$ mag (Schlafly & Finkbeiner 2011) using the Calzetti dust law (Calzetti et al. 2000). Figure 1 shows the Las Cumbres *BgVri* and ZTF *gr* data across all epochs, and Figure 2 shows the same data until +200 days after optical peak to highlight the bulk of the photometry.

There is a systematic difference between the ZTF and Las Cumbres *r*-band magnitudes, due to their filter differences (see the Appendix). ZTF *r*-band magnitudes are on average 0.244 mag brighter than Las Cumbres *r*-band data when generating synthetic photometry from spectra of the TDE. The Las Cumbres and ZTF *r*-band subtracted photometry were found to always agree within this range across epochs, but for visual purposes, the ZTF data are shown corrected for this offset to match the Las Cumbres data in the figures better.

The Las Cumbres data show a bump in the *i* band (at +83 days as seen in Figure 2) and late-time emission can be seen, neither of which are typical of TDEs. We expand on the implications of these observations in Section 4.

2.2. Swift Photometry

UV observations were obtained with the Ultraviolet Optical Telescope (UVOT; Roming et al. 2005) from Swift in the *UVW*2, *UVM*2, *UVW*1, and U filters beginning MJD 59,075.14 (PI: Gezari), near the time of maximum light. The data were reduced with the Swift Ultraviolet/Optical Supernova Archive pipeline (Brown et al. 2014), using the aperture corrections and zero-points of Breeveld et al. (2011). Despite low contamination expected from the UV-dim host galaxy, host subtraction was performed with templates taken on 2022 March 26 (MJD 59,664.0). Swift photometry is presented in Vega magnitudes alongside the Las Cumbres and ZTF photometry in Figures 1 and 2.

Swift's X-ray Telescope (XRT) simultaneously observed AT 2020mot during UVOT follow up. Following the Swift XRT Data Reduction Guide,[13] we processed cleaned X-ray event files with `xselect`[14] to create a light curve binned by

---

[10] https://github.com/LCOGT/lcogtsnpipe

[11] https://github.com/acbecker/hotpants

[12] https://ztfweb.ipac.caltech.edu/cgi-bin/requestForcedPhotometry.cgi

[13] https://www.swift.ac.uk/analysis/xrt/files/xrt_swguide_v1_2.pdf

[14] https://www.swift.ac.uk/analysis/xrt/xselect.php

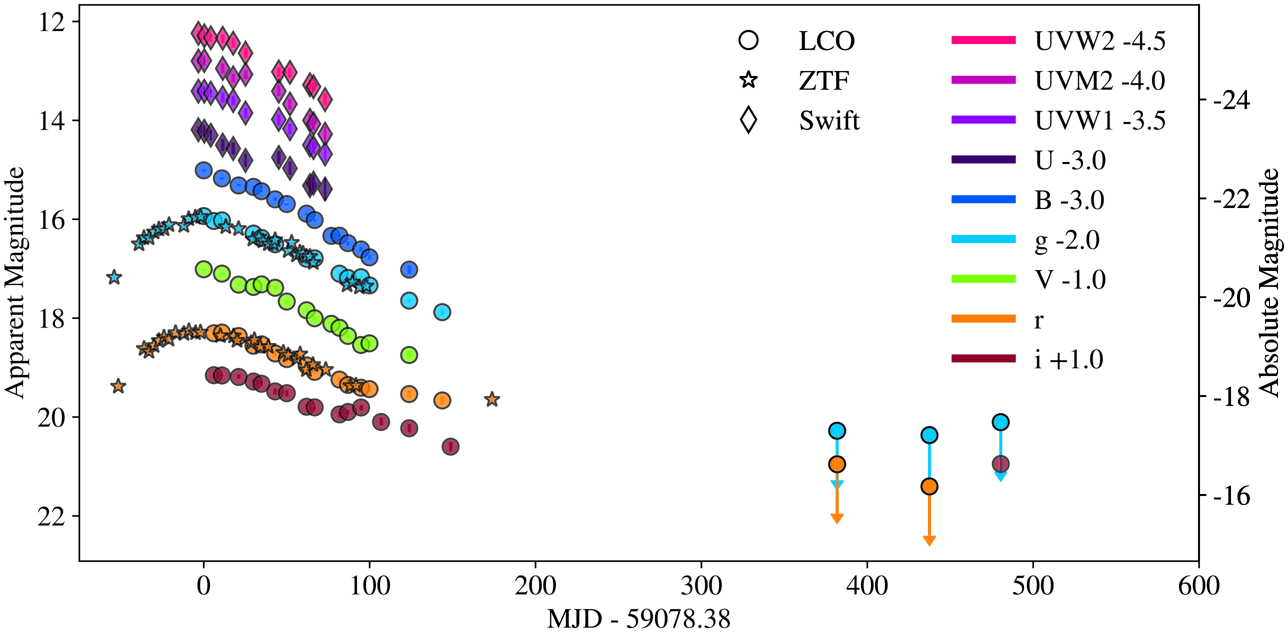

Figure 1. The host-subtracted and Galactic-extinction-corrected optical and UV light curves of AT 2020mot as observed by Las Cumbres Observatory, ZTF, and Swift. The light curve in each filter is offset from one another for clarity, and the ZTF *r* band is further offset by 0.244 mag to account for the systematic difference between the ZTF and Las Cumbres *r*-band filter curves (see the Appendix). The *gri* points from Las Cumbres were subtracted with PS1 archival templates (MJDs 55,914.0, 55,957.0, and 55,991.0, respectively) including the epochs +200 days from *g*-band peak which show residual TDE flux.

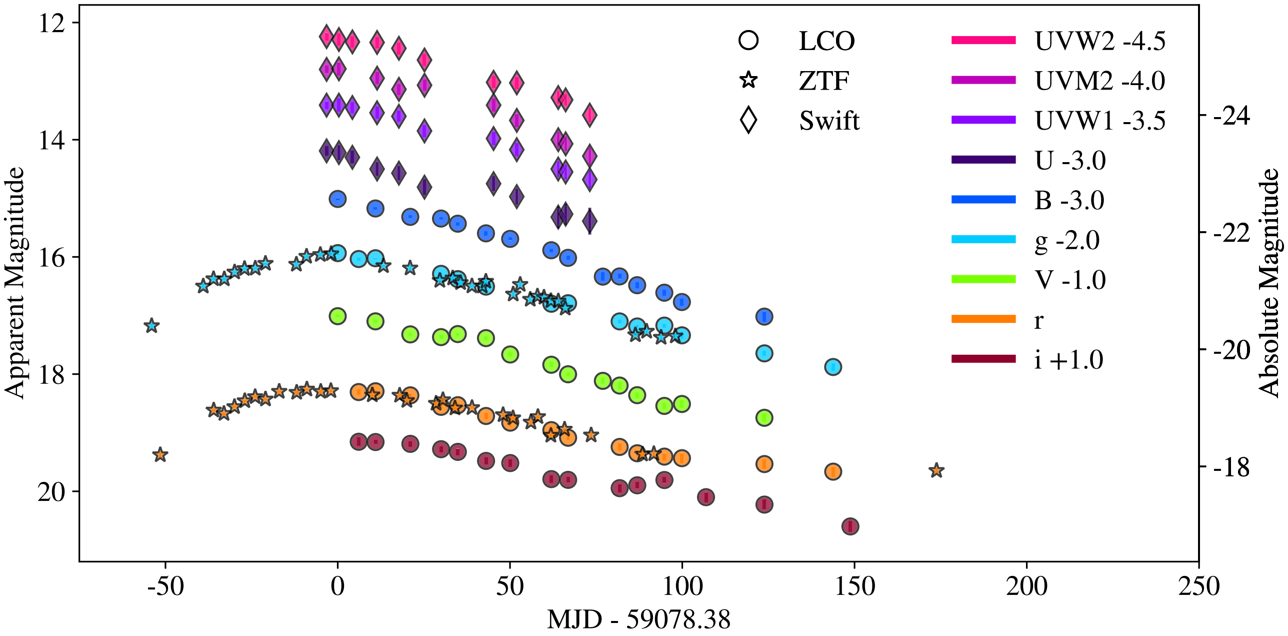

Figure 2. Same as Figure 1, excluding the epochs +200 days to show the first optical peak clearly.

an exposure time of 2 ks. In this case, zero counts were measured across all observations, so only upper limits are inferred. We display these upper limits alongside the bolometric luminosity (see Section 3.2) of AT 2020mot in Figure 3. These results are in agreement with the findings of Hammerstein et al. (2023).

2.3. WISE photometry

The host galaxy of AT 2020mot, WISEA J003113.52+850031.8, was first observed by WISE in its NEOWISE survey in 2010, and its observations resumed in 2013 when the survey was reactivated as NEOWISE-R (Mainzer et al. 2011). We collected *W1* (3.4 μm) and *W2* (4.6 μm) data from the Infrared Science Archive,[15] resulting in 20 epochs of MIR photometry each separated by six months, five of which were taken after the TDE flare.

WISE data were parsed for detections with good-quality frames (qi_fact > 1), no contamination and confusion (cc_flag = 0), and with magnitude errors < 0.15 mag; these requirements filtered out ∼10% of the observations across all epochs. Figure 4 shows the time-resolved coadded fluxes of the field created as part of the unWISE project (Lang 2014; Meisner et al. 2018) in both bands, with data shown before and

---

[15] https://irsa.ipac.caltech.edu

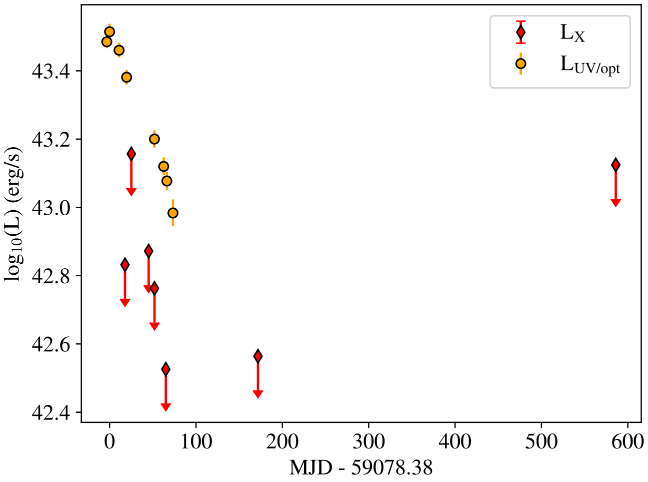

Figure 3. The upper limits of X-ray luminosity from nondetections of AT 2020mot from Swift's XRT (red filled diamonds), compared with the bolometric luminosity inferred from blackbody fits to the UV/optical light curve (orange filled circles). The X-ray upper limits show a maximum of 1.33×10^{43} erg s^{-1} throughout the UV/optical flare.

after the onset of AT 2020mot. With a custom code (De et al. 2020) based on the ZOGY algorithm (Zackay et al. 2016), we also subtracted the NEOWISE images using the full-depth coadds from 2010 to 2014 as reference images and obtained forced PSF photometry at the transient position on the subtracted WISE images to determine the transient-specific flux for the epochs after the peak of AT 2020mot (MJD 59,078.38), shown in Figure 5 with *gri*-band photometry from Las Cumbres shown for comparison.

The first two epochs after TDE detection in both the *W*1 and *W*2 filters are still within 1σ of the quiescent stage. However, the latter three epochs exceed the quiescent flux by at least 1σ, and the peak luminosity of the posttransient subtracted fluxes are $L_{W1} = 2.11 \pm 0.11 \times 10^{40}$ erg s^{-1} and $L_{W2} = 9.27 \pm 1.18 \times 10^{39}$ erg s^{-1}.

2.4. Spectroscopy

Optical spectra were taken with FLOYDS on Las Cumbres's 2 m Faulkes Telescope North (FTN) on Haleakalā, HI, reduced using the `floydsspec` pipeline,[16] as described in Valenti et al. (2014). The pipeline performs flux and wavelength calibration, cosmic-ray removal, and final spectrum extraction. The original spectra cover 3500–10000 Å, at a resolution $R \approx 300$–600 and epochs from −3 to +46 days with respect to the *g*-band peak at MJD = 59,078.38, calculated by fitting a template TDE light curve to the observations with a least-squares method and finding the time of maximum light from the template. We subsequently obtained a host spectrum at +726 days after peak. The dates and phases of each spectrum we report are listed in Table 1.

Each spectrum was taken at airmass > 2.3, compared to airmass = 1.8–2.0 for the photometry. We present spectra without host subtraction in Figure 6, and with the host spectrum, taken 726 days after the peak of AT 2020mot, presented alongside for comparison.

In Figure 7, we also show the six epochs of AT 2020mot spectra after host subtraction via calibration to match the host-subtracted *BgVr* photometry. We first subtracted the host spectrum from each transient epoch multiplied by a factor that minimizes the difference between the synthetic photometry and the real host-subtracted photometry of the corresponding epoch using the sum of all bands. We then divided between this host-subtracted synthetic photometry and the observed

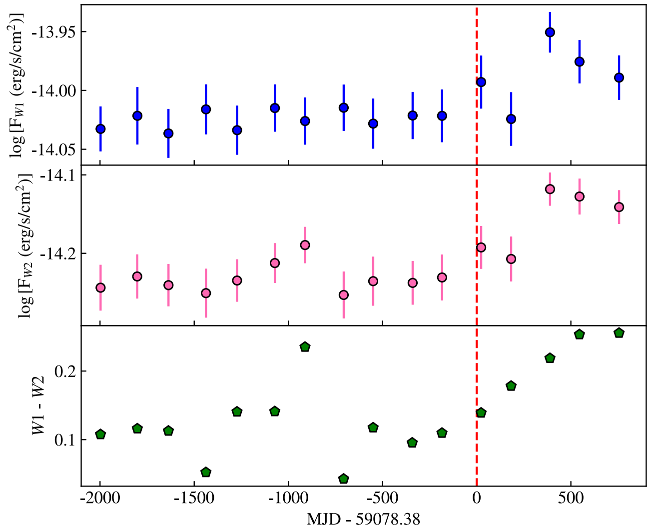

Figure 4. NEOWISE observations at the location of AT 2020mot in the *W*1 (top panel) and *W*2 (middle panel) IR bands. The coadded flux of each epoch is in blue (*W*1) and pink (*W*2). The vertical dashed red line denotes the time of the first optical detection of AT 2020mot. The bottom panel shows the *W*1 − *W*2 color, which never reaches AGN levels.

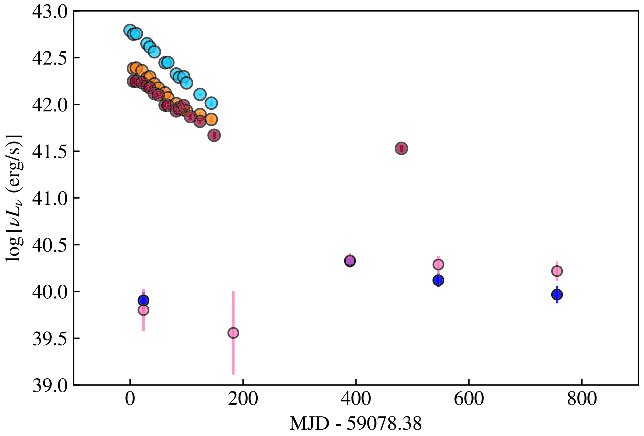

Figure 5. The host-subtracted luminosities in the *W*1 (blue pentagons) and *W*2 (pink pentagons) IR bands, shown alongside Las Cumbres and ZTF *gri* (cyan, orange, and red circles, respectively) subtracted photometry for reference relative to *g*-band peak. Only one epoch in each band of WISE photometry, before 2022, shows significant excess flux compared to the pre-TDE quiescent stage (the second pre-2022 epoch is within the errors of the quiescent stage).

Table 1
The MJD and Phase at Which Each Reported Spectrum Was Taken by FLOYDS-FTN, Where the Phase is the Number of Days from Peak in the *g* Band (at MJD 59,078.38)

MJD	Phase	Airmass	Exposure Time (s)
59,074	−3	2.31	3600
59,084	+7	2.31	3600
59,092	+15	2.32	3600
59,105	+28	2.32	3600
59,117	+36	2.32	3600
59,119	+46	2.31	3600

---

[16] https://github.com/svalenti/FLOYDS_pipeline/

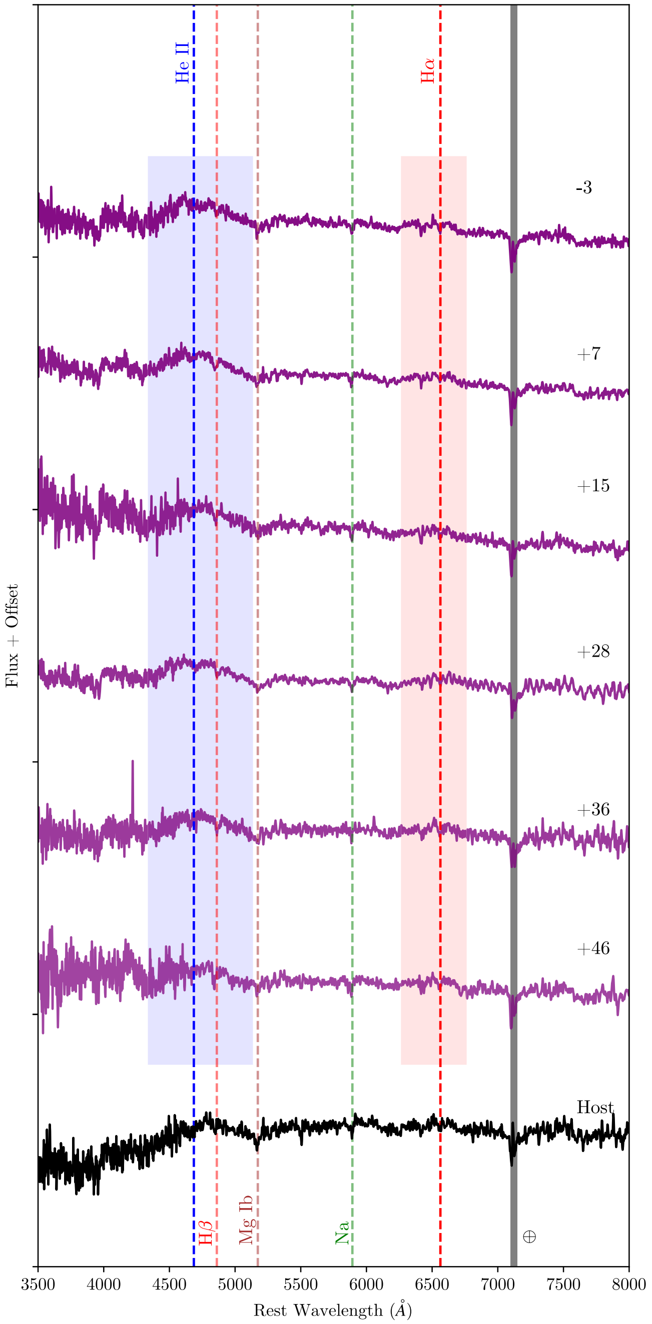

Figure 6. AT 2020mot and host spectra from Las Cumbres' FLOYDS-FTN. All spectra have been corrected for Galactic extinction. Six epochs during the tidal disruption (purple lines) range from 3 days before g-band peak to 46 days after, offset for visual clarity, and a host spectrum (obtained 726 days after peak) is shown below (black line). The vertical dashed lines mark characteristic lines from the TDE and host, with Hα and Hβ in red, He II λ4686 in blue, and host Na λ5890 and the Mg Ib λλλ5167, 5172, 5183 triplet in green and brown, respectively. The shaded regions indicate the breadth of Hα and He II. We also label the telluric contamination.

photometry, resulting in scale factors at the central wavelength of each filter. We interpolated between these filter-specific scale factors using a linear spline to give scale factors across all wavelengths. We multiplied the spectrum by these interpolated scale factors to get the final calibrated spectrum, again minimizing the difference between the synthetic and observed photometry at each iteration by using `scipy.optimize.minimize`. Final calibrated spectra are shown in Figure 7. Finally, we present a comparison of AT 2020mot to the classification spectrum of AT 2018fyk in Figure 8. AT 2018fyk is a TDE with broad He II λ4686 (Wevers et al. 2018, 2019), thus similar in classification to AT 2020mot.

3. Observational Results

We assess the multiband photometric data by comparing the light curve's NIR peculiarities against a broad sample of optical TDEs, calculating blackbody radii and temperatures of the event across epochs, and modeling the light curve with two TDE emission mechanisms to determine the masses of the central BH and the stellar progenitor.

3.1. NIR Excess and Bump

The i-band data are brighter than expected across all epochs and show a "bump" starting at MJD = 59,160 (+83 days after peak). The peak of this bump is approximately 100 days after maximum light in the g band.

Color evolution illustrates AT 2020mot's unique red excess, as well. In Figure 9 we present AT 2020mot's $g-r$ and $r-i$ colors at each epoch, against a backdrop of the respective median colors of 15 archival TDEs with gri photometry for 80 days after first detection: AT 2017eqx and AT 2019qiz, (Nicholl et al. 2019); AT 2018hyz (Gomez et al. 2020); AT 2018hco, AT 2019bhf, AT 2019cho, AT 2019dsg, AT 2019 ehz, and AT 2019meg (van Velzen et al. 2021b); AT 2018iih (Gomez et al. 2020); PS1-10jh (Gezari et al. 2012, 2015); PS1-11af (Chornock et al. 2014); PTF09ge (Arcavi et al. 2014); iPTF16axa (Hung et al. 2017); and iPTF16fnl (Blagorodnova et al. 2017). Las Cumbres is the only telescope contributing i-band photometry for AT 2020mot. While AT 2020mot progresses overall in agreement with the background sample in $g-r$ color without unusual evolution, it has a high $r-i$ color compared to the sample throughout the entire light-curve decline, as well as increasing to the reddest colors at the time of the bump.

3.2. Light-curve Fitting

We fit the UV and optical spectral energy distributions (SEDs) of AT 2020mot with a blackbody across its light curve to estimate the evolution of the photospheric radius and temperature. We exclude the i-band data from these fits as we interpret their excess brightness and late-time bump as an indication of contribution from a dust echo (see Section 4). We use only epochs across with five or more filters of data within 2 days in the `lightcurve_fitting` package from Hosseinzadeh & Gomez (2022), ensuring that only epochs with UV data from Swift will be used to avoid underestimating the temperature (see Arcavi 2022). The code uses Markov Chain Monte Carlo (`MCMC`) sampling with the `emcee` package (Foreman-Mackey et al. 2013) with a broad log-flat prior of $10{,}000\ \mathrm{K} \leqslant T \leqslant 100{,}000\ \mathrm{K}$ and $10\,R_\odot\ (\sim 10^{-7}\ \mathrm{pc}) \leqslant R \leqslant 10^6\ R_\odot\ (\sim 10^{-2}\ \mathrm{pc})$.

Though this package provides 16–84 percentiles as the errors on the estimated parameters (which are plotted for reference in Figure 10), we quantify our temperature measurements with the uncertainties found in Arcavi (2022) for the bounds on light-curve fits to blackbodies with UV and optical data. Thus we find the temperature declines slowly from $T_{\rm BB} = 14{,}600 \pm 2500$ K to $T_{\rm BB} = 12{,}300 \pm 2500$ K. These temperatures are consistent with,

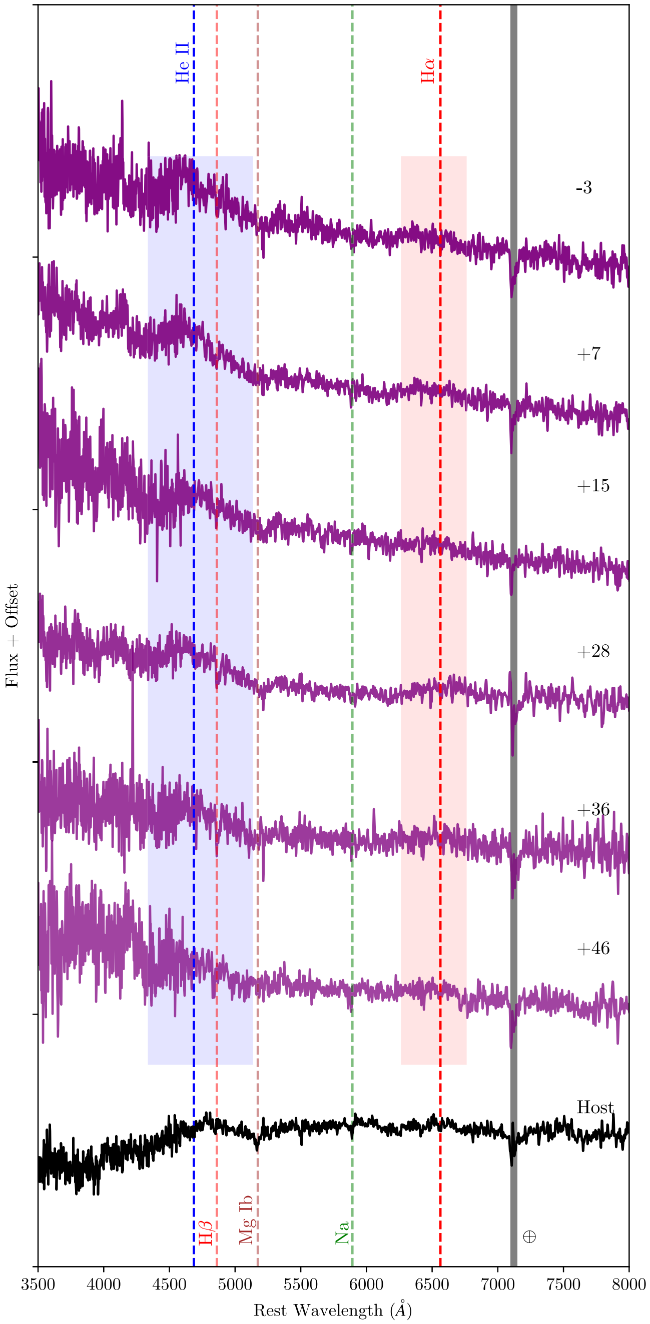

Figure 7. Same as Figure 6, but each epoch of AT 2020mot (purple) has been host subtracted as described in Section 2.4. This process reveals the blue continuum as observed photometrically, typical for TDEs, and further distinguishes the transient features from the host contamination. This calibrating subtraction also highlights the broad He II λ4686 that is present from the TDE and fades by 46 days after peak. However, the subtraction exaggerates noise, especially on the wavelength edges due to red fringing and lower blue resolution, so any features blueward of He II are indistinguishable.

though on the lower end of, other TDE observations (10,000–50,000 K; e.g., van Velzen et al. 2021a). The blackbody radius is simultaneously found to decrease more strongly, from $R_{\rm BB} = 3.16 \pm 0.06 \times 10^{-4}$ pc to $R_{\rm BB} = 2.49 \pm 0.08 \times 10^{-4}$ pc, also consistent with TDE observations (van Velzen et al. 2021a). These parameters give an estimated blackbody luminosity $L_{\rm BB} = 3.05 \pm 0.20 \times 10^{43}$ erg $\rm s^{-1}$ at peak, corresponding to an initial Eddington ratio of ∼0.1 for the average SMBH mass inferred in Section 3.3, $M_{\rm BH} \approx 4.5 \times 10^{6}\ M_{\odot}$, and declining to $L_{\rm BB} = 9.63 \pm 0.83 \times 10^{42}$ erg $\rm s^{-1}$ at late times.

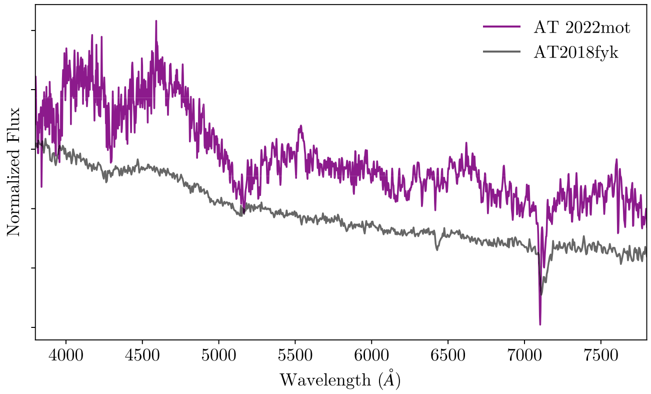

Figure 8. AT 2020mot's host-subtracted spectrum from 7 days after peak (purple) compared to the AT 2018fyk classification spectrum (gray). Both are normalized such that their integrated flux equals 1 for visual comparison. AT 2018fyk is another TDE with broad He II λ4686 (Wevers et al. 2018, 2019).

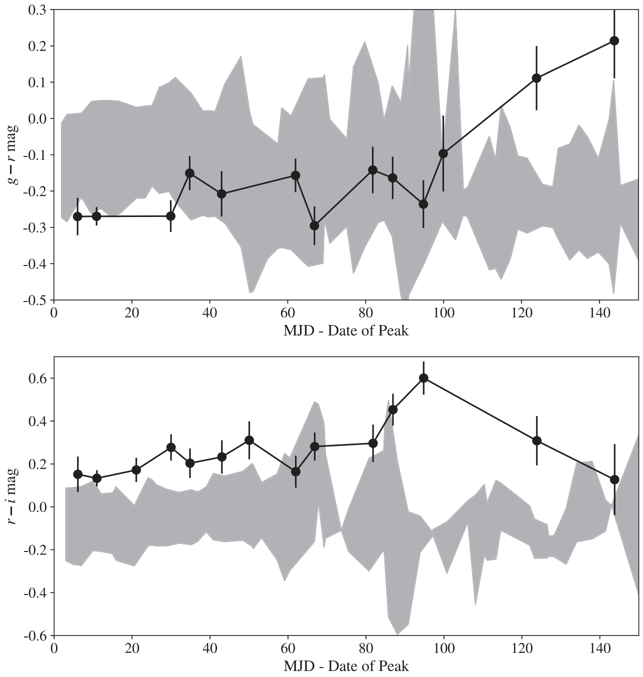

Figure 9. Progression of the $g-r$ (top panel) and $r-i$ (bottom panel) colors of AT 2020mot (black points) and a sample of 15 archival TDEs (gray filled-in section). Dates are shown with respect to each TDE's g-band peak. The archival TDE spread in gray shows the moving median and absolute median deviation of the color among all TDEs at each epoch. AT 2020mot's $g-r$ color is unremarkable until late times, while in $r-i$ it is uniquely red across all epochs and reddens even further at the bump +80 days after peak before declining.

3.3. Black Hole and Predisruption Stellar Masses

Two computational tools are publicly available to determine the mass of the SMBH and predisruption star from TDE light-curve properties. The Modular Open Source Fitter for Transients (MOSFiT;[17] Guillochon et al. 2018), has a TDE

---

[17] https://github.com/guillochon/MOSFiT

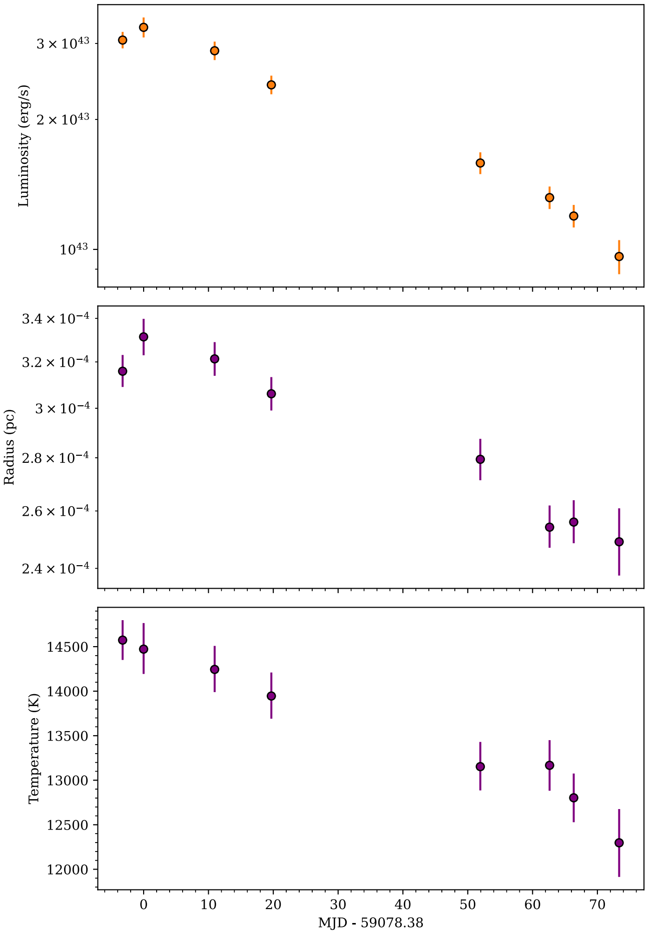

Figure 10. The blackbody temperature (bottom) and radius (middle) as fit from the photometric evolution of AT 2020mot using Swift *UVW*2, *UVM*2, and *UVW*1 and Las Cumbres/ZTF *BgVr* data. The blackbody luminosity is calculated from the fitted parameters as $L = 4\pi R^2\sigma T^4$ and plotted in the top panel.

model that assumes fast circularization of the debris stream and subsequent formation of an accretion disk that is ultimately powering the event (Mockler et al. 2019). Alternatively, TDEMass[18] uses only the peak bolometric luminosity and temperature to determine both the SMBH and stellar mass by assuming the flare is produced from shocks on the debris' circularization path (Ryu et al. 2020). Both methods were applied to our host-subtracted, extinction-corrected light curves which combine all Las Cumbres and Swift contributions.

We first fit the ZTF, Las Cumbres, and Swift combined data, which correspond to the light-curve rise, peak, and decline, with MOSFiT. We used the nested sampling mode and fixed the redshift to the spectroscopically determined $z = 0.07$. In Table 2 we show that MOSFiT finds a best-fit mass of the host galaxy's SMBH to be $M_{\rm BH} = 17.37^{+1.66}_{-1.90} \times 10^6 M_\odot$ and the mass of the star before disruption $M_* = 1.04^{+0.05}_{-0.04} M_\odot$. These results are nearly an order of magnitude larger than found by Hammerstein et al. (2023) ($M_{\rm BH} = 2.95$–$6.91 \times 10^6\ M_\odot$, where the range is from the errors on their results from both MOSFiT and TDEMass). Yao et al. (2023) also find smaller results for AT 2020mot's host black hole mass, $M_{\rm BH} = 2.09$–$10 \times 10^6\ M_\odot$, using their measured velocity dispersion of the host galaxy and the Kormendy & Ho (2013) relation.

Table 2
Black hole Masses Estimated from MOSFiT and TDEMass.

Fitting Tool	Epochs Used	$M_{\rm BH}$ ($10^6\ M_\odot$)	M_* ($M_\odot$)
MOSFiT	Peak + Decline	$17.37^{+1.66}_{-1.90}$	$1.04^{+0.05}_{-0.04}$
TDEMass	Peak	$3.40^{+2.7}_{-1.4}$	$0.75^{+0.09}_{-0.07}$

TDEMass only uses the estimated bolometric luminosity and temperature at peak, instead of the entire observed light curve, to constrain SMBH and stellar mass estimates (Ryu et al. 2020). AT 2020mot's brightest measured bolometric luminosity ($3.05 \pm 0.2 \times 10^{43}$ erg s^{-1}) and corresponding temperature ($14{,}600 \pm 2500$ K) result in an estimated $M_{\rm BH} = 3.40^{+2.7}_{-1.4} M_\odot$ and $M_* = 0.75^{+0.09}_{-0.07} M_\odot$.

3.4. Host Galaxy Properties

The Las Cumbres host spectrum, shown in Figures 6 and 7, shows the Na I D $\lambda\lambda$5890, 5896, Mg Ib λ5175, and Ca H & K $\lambda\lambda$3934, 3968 absorption lines. The relationship between host extinction and the equivalent width of the Na I D doublet has been well established (Munari & Zwitter 1997), but our spectrum is too noisy and lacks the resolution to discern the equivalent width (Poznanski et al. 2012), so we do not estimate host reddening from this process. The spectrum also confirms a galactic environment with a young stellar component from the Balmer absorption lines characteristic of A stars, yet no emission, particularly no [O III] expected from active star formation. The presence of young stars without ongoing star formation is indicative of a recently quenched galaxy, such as a poststarburst or postmerger E + A galaxy (Zabludoff et al. 1996), as found to be the case in many TDEs (Arcavi et al. 2014; French et al. 2016). Furthermore, the detection of the Mg Ib λ5175 and Ca H & K $\lambda\lambda$3934, 3968 absorption lines in the host spectrum reflects an older stellar population. Liodakis et al. (2023) also determine the galaxy to be spheroidal and likely elliptical. Kormendy & Kennicutt (2004) consider elliptical galaxies to be dominated by a classical bulge, thus we expect the stellar mass of the host to be comparable to the bulge mass.

We assess how SMBH mass relations via host galaxy properties compare with analyses from TDE light curves (see Section 3.2) by fitting the available photometric data of the host galaxy WISEA J003113.52+850031.8 (Skrutskie et al. 2006), as listed in Table 6, with the SED fitting code `BAGPIPES` (Carnall et al. 2018). For further detail on our use of this fitting tool, see the Appendix.

The mass formed from the best-fit double power law is $\log_{10}(M_*/M_\odot) = 10.02^{+0.05}_{-0.03}$. If taking the stellar mass formed to equate the bulge mass, we can use the relation between the bulge mass and SMBH mass for TDEs from Ramsden et al. (2022),

$$\log_{10}\left(\frac{M_{\rm BH}}{M_\odot}\right) = 7.0 + 0.18\log_{10}\left(\frac{M_{\rm bulge}}{10^{11} M_\odot}\right), \qquad (1)$$

which was derived using a sample of 32 TDEs whose BH masses were determined with MOSFiT only (Nicholl et al. 2022), and gives Ramsden et al. (2022) $M_{\rm BH} = 6.66 \times 10^6\ M_\odot$.

The value determined from the TDE-specific Equation (1) falls between that found from our own MOSFiT run and TDEMass fit to the light curve of AT2020mot. However, the relation was itself calibrated to MOSFiT-determined BH

---

[18] https://github.com/taehoryu/TDEmass

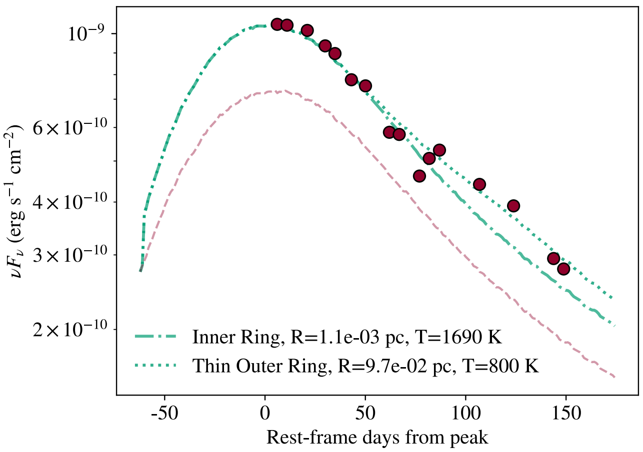

Figure 11. The observed i-band light curve (red filled circles) compared with the estimated intrinsic emission (red dashed lines) alongside the inclusion of dust reemission (blue dashed and dashed–dotted lines). The best-fit light curves from dust reprocessing are a thin inner ring at 0.001 pc (dashed–dotted line) from the central SMBH, and another ring at 0.09 pc (dashed line).

Table 3
Estimates of BH Mass from Relations Using Host Galaxy Properties

Relation	Source	M_{BH}
		(10^6 $M_\odot$)
$M_{\rm BH}$–$M_{\rm bulge}$	Ramsden et al. (2022)	6.66
$M_{\rm BH}$–L_V	Kormendy & Ho (2013)	1.36 ± 0.38

masses. Similarly, the bulge mass may be overestimated from tools like `BAGPIPES` whose models are based on galaxy samples of higher masses, and by assuming the stellar mass is equal to the bulge mass.

Another estimate for SMBH mass uses a scaling with the host galaxy's luminosity. Using archival Two Micron All Sky Survey (2MASS; Skrutskie et al. 2006) images of the host galaxy to determine the host K-band luminosity 2.16×10^{42} erg s^{-1}, (listed in Table 6), the relation from Kormendy & Ho (2013),

$$\log_{10}\left(\frac{M_{\rm BH}}{M_\odot}\right) = 8.734 + 1.21\log_{10}\left(\frac{L_{K,\rm bulge}}{10^{11}L_{K,\odot}}\right), \quad (2)$$

gives $M_{\rm BH} = 1.36 \times 10^6$ $M_\odot$, a lower estimated value compared to the $M_{\rm BH}$–$M_{\rm bulge}$ relations, but in closer agreement with the mass determined by TDEMass. Both mass estimates from host galaxy modeling are listed in Table 3.

4. Circumnuclear Dust Models

The brightness of AT 2020mot in the i band exceeds that of other optical TDEs (see Figure 9) and shows a rebrightening bump after MJD 59,160, starting 83 days after maximum light. We explore whether models of circumnuclear dust can explain the observations as a "dust echo" of delayed, reprocessed emission. Past works on potential dust echoes in TDEs have relied almost solely on WISE data, and none discuss the possibility of an echo being observed in the i band (e.g., Jiang et al. 2016a, 2017, 2021; Dou et al. 2016; van Velzen et al. 2016; Li et al. 2020; Stein et al. 2021; Onori et al. 2022; Wang et al. 2022).

We use the methods of van Velzen et al. (2016) to model the response light curve in the IR bands from dust grain absorption of UV to optical light. The reprocessed light is dominated by the peak emission, especially in our case of i-band excess which occurs within 3 months of the optical peak, thus we use the light curve of the g band shifted to match the peak brightness of the bolometric luminosity to model the light that is being reprocessed. However, Yao et al. (2023) determine AT 2020mot to have a power-law decline followed by a late-time plateau; therefore, the near-constant optical brightness at late times from the TDE could impact longer-term IR signatures, which may be visible in WISE photometry that is not yet publicly available. See Sections 2 and 4 of van Velzen et al. (2016) for specifics of the response function based on assumptions of the type and size of the dust grains, and the parameterization of dust geometries around the SMBH. Assuming spherically symmetric TDE emission and a graphite[19] dust grain of radius $a \sim 0.1$ μm, we begin with the generic model,

$$L_{\nu,\rm echo} \propto \int \Psi(\tau) L_{\rm TDE}(t - \tau) d\tau, \quad (3)$$

where Ψ is the response function of the dust and $L_{\rm TDE}$ is the integrated UV and optical luminosity measured at time $t - \tau$, with t being the time of IR detection and τ being the delay between when the TDE light was emitted and when it was reprocessed to IR based on the distance R and angle θ of the dust from the TDE. van Velzen et al. (2016) parameterize τ with respect to a polar axis aligned to the observer's line of sight, such that,

$$\tau = \frac{R}{c}(1 - \cos\theta). \quad (4)$$

With this framework, the light curve expected from a thin spherical shell of dust is modeled as,

$$L_{\nu,\rm echo} = A C_q B_\nu' 2\pi \int_0^\pi L_{\rm TDE}(t - \tau)\sin\theta d\theta, \quad (5)$$

where A is a constant of amplification reflecting the ratio between observed IR luminosity and the amount calculated from reprocessing and B_ν' is a modification of the Planck function B_ν, which encodes the IR-specific response to the absorbed UV and optical luminosity, such that $B_\nu' = B_\nu \nu^q$ (van Velzen et al. 2016). Maintaining the assumption of dust grains of size $a \sim 0.1$ μm, Draine & Lee (1984) gives $q = 1.8$ and C_q is a constant of normalization $C_q = 1\big/\int B_\nu' d\nu$.

This model can be adjusted for including shell thickness by including integration over extended radii,

$$L_{\nu,\rm echo} = C_q 2\pi \int_{R_0} \int_0^\pi L_{\rm TDE}(t - \tau)\sin\theta \times A \times n(R) B_\nu'(T(R)) d\theta dR. \quad (6)$$

The amplification factor A remains in the integral in cases of radial thickness because it can vary at each radius. We can thus also evaluate the thick shell models with varying densities $n(R)$ of dusty material at each radius step, and account for temperature variation with increasing radius as $T(R) = T_0(R/R_0)^{-0.345}$ (van Velzen et al. 2016).

Furthermore, by restricting the angular variation, we can mimic a ring (all dust at one inclination angle and radius), thick ring (superposition of rings at increasing radii), and torus

---

[19] Silicate grains have a much lower sublimation temperature such that any present would not last to reprocess the emission from a UV/optical flare.

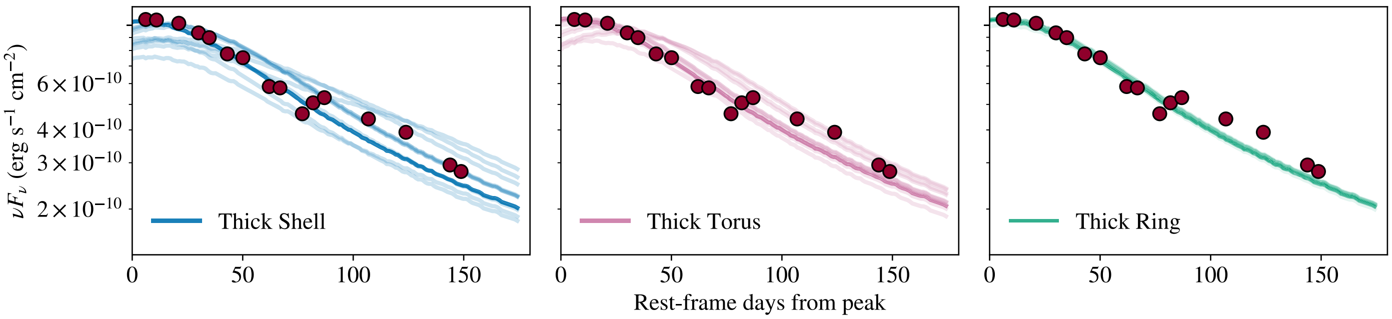

Figure 12. Posteriors of the reprocessed emission from different thick-dust geometries with Bondi density profiles alongside the *i*-band excess (shown in red filled circles). The left panel shows the posteriors for a shell in blue lines; the middle panel shows those of a torus in red lines; and the right panel shows those of a ring in green lines. A varying radius directly delays the onset of the enhanced emission, while a varying temperature affects the amplitude of the reprocessing.

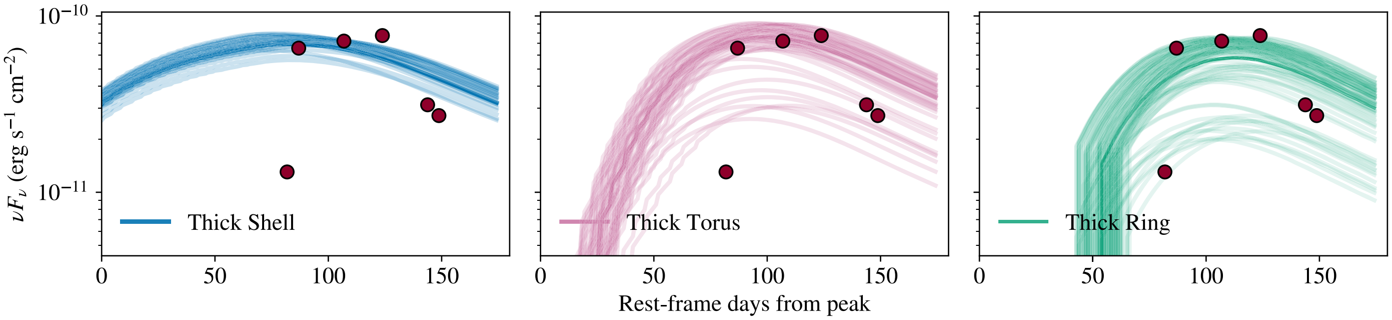

Figure 13. Same as Figure 12, but for the photometry points and dust model fitting only correspond to the bump in the *i*-band brightness beginning after 80 days from the optical peak.

geometry (small central segment of the spherical shell at one inclination angle and superimposed radii). For instance, a face-on thick ring would be modeled with,

$$L_{\nu,\mathrm{echo}} = 2\pi \int_{R_0} A C_q n(R) B_\nu^{'}(T(R)) L_{\mathrm{TDE}}(t-\tau)\, dR, \qquad (7)$$

because all IR emission follows the same time delay without angular dependence such that $\tau = R/c$ in the face-on case. By extension, a ring or torus at a different inclination would also integrate over angular dependencies.

We test six fiducial geometries of dust: thin spherical shell, thick spherical shell, face-on thin ring, face-on thick ring, face-on thin torus, and face-on thick torus. The cases of radial thickness are also tested with both constant and Bondi density ($n(R) \propto R^{-3/2}$) profiles. We then perform MCMC fitting to estimate the best-fit combination of distance R from the SMBH (with log priors over 10^{14}–10^{18} cm), its temperature of reemission T (flat priors over 100–5000 K), and the amplitude of reprocessing (flat priors over 0.001–10) for each configuration of dust whose reemission could match and the observations. The *i*-band data are separated into "prebump" (MJD < 59,150.0) and "bump" (MJD ≥ 59,150.0) groups. We begin with prebump data, and make the significant assumption that the intrinsic *i*-band luminosity follows what would be expected with the application of the PS1-10jh template (Gezari et al. 2012), shifted to match the luminosity difference found for AT 2020mot between the *g* and *r* bands. This assumed intrinsic luminosity can be seen in Figure 11 and is subtracted from the observed prebump luminosity measurements, to isolate the light that is in excess from the TDE flare and thus likely a result of dust reprocessing.

The *i*-band light curve is consistent with the expected intrinsic TDE emission combined with reprocessed emission of two face-on rings each with a Bondi density profile. The innermost radius of the first ring is $R_{\mathrm{sub}} = 1$–5×10^{-3} pc with a temperature of $T \approx 1700$ K, and the radius of the second ring is at $R_{\mathrm{sub}} = 9.7 \times 10^{-2}$ pc with a temperature of $T \approx 800$ K, as shown in Figure 11. These values are determined from the results with the highest likelihood scores after MCMC fitting, instead of using the median of the fit, because of the varied degree of convergence for each parameter.

In Figures 12 and 13, the results from this fitting process for different geometry examples are presented for both the prebump and bump data points. There is little difference between the scenarios of a spherical shell, ring, or torus at similar scales in generating enough reprocessed light to match the observations before the bump. The bump, however, is not uniformly fit by all geometries. The spherical shell models produce flatter, wider reprocessing light curves (described as "square waves" in van Velzen et al. 2016) due to the different distances at which light will have to travel from the origin at the TDE to the surrounding dust at different angles. The more centrally located the dust is along the plane perpendicular to our line of sight (that is, the closer to a face-on ring or torus), the more the reprocessing emission is received as a steeper and sharper light curve. As this qualitatively describes a bump, we expected ring and torus configurations to be responsible for the bump, and confirm as follows.

To fit the luminosity of the bump that is only from a secondary dust reprocessing, the luminosity from the first dust grouping (sphere, ring, or torus) is subtracted from the observed bump points. We test only superpositions of like geometries: inner and outer shell; inner and outer ring; and inner and outer torus. Figure 11 also shows the best-fit light curve to the bump, which is provided by an outer ring at $R = 0.09$ pc with a lower temperature than the inner ring. Inner and outer torus configurations were best fit at the same radii, however, the outer torus produces an ultimately flatter light curve than the outer ring, leaving the ring to match the observed bump best, as

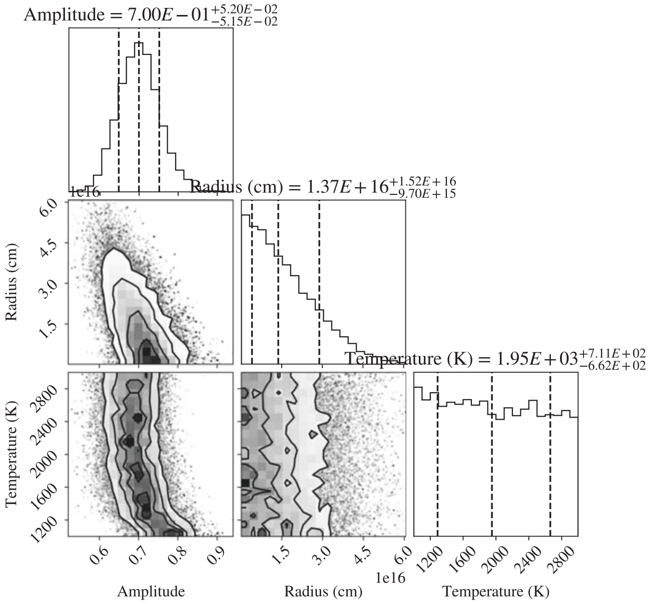

Figure 14. Corner plot showing the convergence of the ring dust model's fitting parameters for the excess in i-band brightness at early times.

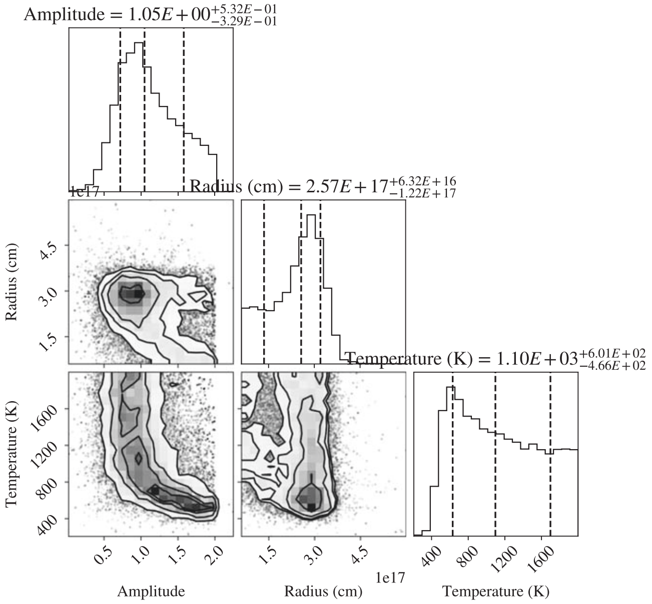

Figure 15. Corner plot showing the convergence of the ring dust model's fitting parameters for the bump in i-band brightness beginning after 80 days from the optical peak.

shown in Figure 13. No spherical shell model was found to fit the bump data, as the flatter reprocessing light curve from a sphere would also contribute luminosity to the prebump phase. Concentric spherical shells are thus unlikely to explain the early i-band excess and late-time bump. Figures 14 and 15 show the corner plots for the fits to inner and outer rings, also showing that the inner ring of dust is matched by the smallest of scales such that the radius solution does not converge at the median value, while the temperature solution is not converged and the results are unaffected by temperature variance.

We show the effect of our best-fit concentric rings of thin dust in the MIR by showing the reprocessing signatures in the WISE $W1$ and $W2$ bands alongside the host-subtracted WISE epochs of AT 2020mot in Figure 16. Only two epochs overlap in time with the expected reprocessing output of the two rings, and the signatures are indeed within the errors of both of these epochs. Furthermore, we show that a third ring at $R = 0.37$ pc can also reproduce the last three epochs of WISE photometry within the errors.

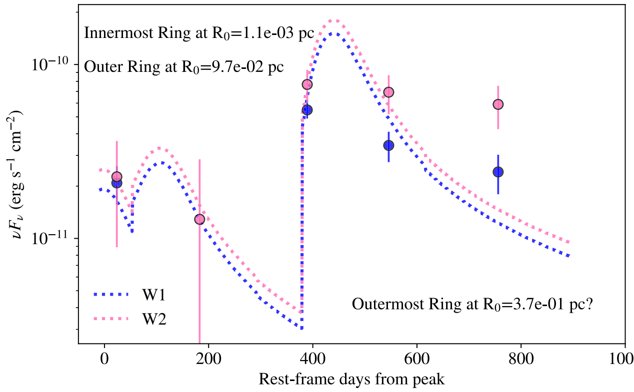

Figure 16. The reprocessing signatures of the inner ($R = 0.001$ pc) and outer ($R = 0.09$ pc) dust rings which best fit the i-band data, in $W1$ (blue) and $W2$ (pink) alongside the subtracted WISE light curves for AT 2020mot. The first two rings produce signatures which overlap within the errors of the $W2$ data, and overlap with the first epoch of $W1$ data. We also show that the latter three epochs of both WISE bands may be explained by a third, outermost ring at $R = 0.37$ pc, but the final epoch is brighter than predicted from this ring, so more complete modeling is needed.

By calculating the dust covering factor f_c as $L_{\text{dust, max}}/L_{\text{TDE, max}}$, where L_{TDE} is the maximum luminosity of the TDE integrated over the UV and optical wavelengths, we also find an inner ring covering factor of $f_c = 4.5\%$ and an outer ring covering factor of $f_c = 0.82\%$.

We explore the physical sensibility of these models and the implications of low covering factors in Section 5.

5. Discussion

We discuss the implications of two possible explanations for the i-band excess and bump in AT 2020mot: dust echoes and extended red emission (ERE).

5.1. Dust echoes: Concentric Rings?

The dust fits to the i band, in addition to the best-fit model's consistency with the WISE data, make AT 2020mot the first TDE with multiwavelength signatures consistent with concentric rings of dust as represented in Figure 17, as well as the first TDE with dust as close as 0.001 pc to an SMBH.

i-band excess and bump have not yet been reported in other TDEs. Enhanced or late-time IR emission in TDEs has been limited mostly to observations from WISE, whose sparse sampling compared to the lifespan of the TDE limits our ability to constrain the geometry of the IR-enhancing material. The Las Cumbres i band is used simultaneously with optical follow up to ensure thorough multiband coverage of the light curve. This early and rapid NIR follow up can uncover dust at previously unreachable subparsec scales near the SMBH, as is the case with AT 2020mot.

Our analysis of the i-band light curve finds that the prebump and bump phases are both well fit by two circumnuclear rings of dust. Face-on disks of dust are physically sensible phenomena to occur around SMBHs, although a torus is more commonly invoked, particularly for AGN (Barvainis 1987; Jiang et al. 2016a; van Velzen et al. 2016). When discussing common dust

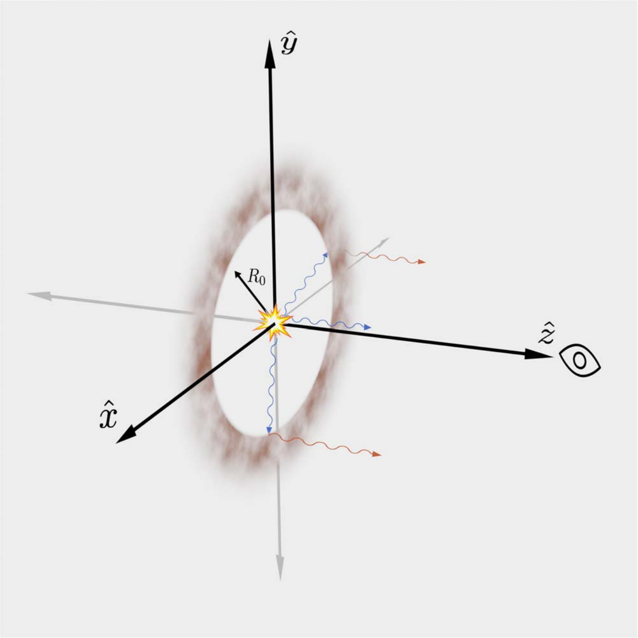

Figure 17. Schematic representation of the ring model of dust surrounding an SMBH, in which the dust lies mostly in the plane facing the observer. Light from the central TDE is emitted isotropically, thus the observer sees unobscured light from the flare along the line of sight. TDE light that is emitted perpendicular to the line of sight meets the ring of dust that is densest at the innermost radius R_0, and the density of dust radially outward decreases following a Bondi profile. This dust absorbs the UV and optical light, and dust that is not sublimated will reprocess the absorbed light into the IR, thus sending a second pulse of light to the observer in the IR only.

configurations around SMBHs, it is important to note differences in the scale and mass of the dust as typically found via reverberation mapping. AGN tori are usually found on scales around ∼0.01–1 pc from the central SMBH, but with a wide range in outer radius extent (Koshida et al. 2014; Minezaki et al. 2019). Disks and rings, however, are more likely in cases with low dust covering factors, because a torus needs a high accretion rate to be sustained (van Velzen et al. 2016). Such disks, if face on, would reprocess oncoming UV and optical light with equal delay times at every azimuthal angle, producing a pulse of enhanced NIR light. If close enough to the initial flare near the SMBH, this light would add to the intrinsic light of a TDE's decline in a corresponding IR filter.

We find concentric rings at $R_1 = 0.001$ pc and $R_2 = 0.09$ pc (see Figure 11) simultaneously fit the prebump and bump light curves. Our models give a maximum dust luminosity of 5.38×10^{41} erg s^{-1} for the inner ring, and 9.75×10^{40} erg s^{-1} for the outer ring. Furthermore the covering factors of 4.5% and 0.82% at each ring are in agreement with other TDE dust covering factors around $f_c \sim 1\%$ (Jiang et al. 2021), and they are orders of magnitude lower than the covering factors found for typical AGN (Barvainis 1987). van Velzen et al. (2016) and Jiang et al. (2016a) note that these low covering factors imply far too little dust for torus formation, and more likely correspond to geometrically thin configurations such as rings.

5.2. Alternative Explanation: ERE?

ERE is a broad emission feature seen in some diffuse systems that is due to the absorption and reemission of UV photons by unidentified dust grains, with measured observations peaking anywhere from 600 Å for the diffuse interstellar medium (Szomoru & Guhathakurta 1998) to 7500 Å for H II regions (Sivan & Perrin 1993). Smith & Witt (2002) also found that the ERE peak wavelength increases with increasing density of the radiation field that excites the dust. This correlation requires an evolving size distribution of the reemitting dust particles by gradual photofragmentation reducing the number of smaller particles.

ERE was reported for Sgr A* by Ghez et al. (2005), posited as evidence of a dust cloud that would have otherwise been pulled into a ring around the SMBH by tidal interactions if it were too physically close; thus it was inferred that the dust was more likely a cloud along our line of sight to Sgr A*. ERE has also been found near other galactic nuclei such as NGC 4826 in H II regions matching the expectation of dust lanes (Pierini et al. 2002).

There is little study on ERE in other galaxies, and much debate on the particles that produce the emission, with polycyclic aromatic hydrocarbons and nanodiamonds being among the top contenders (Chang et al. 2006; Rhee et al. 2007). However, the broad properties of ERE that strongly depend on environmental factors, such as the density of the dusty material and intensity of the radiation field, all make ERE a possible explanation for the anomalous *i*-band emission of AT 2020mot. Since the Las Cumbres *i* band peaks near 7500 Å the excess IR emission of AT 2020mot is indeed similar to that observed for Sgr A* and NGC 4826.

Further studies are needed to assess whether the UV output of TDEs are adequate to explain ERE, and how close the candidate particles responsible for ERE can survive in galactic nuclei.

6. Conclusions

AT 2020mot is a UV/optical TDE in a galaxy at $z = 0.07$. Its light curve is comparable to well-sampled optical TDEs such as PS1-10jh (Gezari et al. 2012), except in the *i* band, which is more luminous than expected and shows an extra "bump" in brightness along the decline. The host properties fit an "E + A" or "K + A" classification that is possibly poststarburst, and/or a product of past mergers (Zabludoff et al. 1996). The association between E + A galaxies and TDEs has been well established since first reported by Arcavi et al. (2014). The host galaxy properties, UV/optical light curve, lack of X-rays (see Figure 3), and radio upper limits of 27 μJy at 15 GHz as reported in Liodakis et al. (2023) all make AT 2020mot an otherwise typical optical TDE, if not for its *i*-band light-curve peculiarities.

The light-curve properties and host galaxy photometry of AT 2020mot indicate a central black hole mass of $M_{\rm BH} \approx 3$–$6 \times 10^6\ M_\odot$, and stream shocks and accretion disk reprocessing models both find masses that are within one another's range of error. Relations between host galaxy properties and black hole mass are historically informed by larger-mass black holes, and thus predict larger black holes as well. However, nearly all our results are consistent with a mass that is $<10^7\ M_\odot$.

We find that the unique *i*-band signatures may be explained by models of two concentric rings of face-on dust reprocessing the TDE emission into the IR. These modeled rings are inferred at distances of 0.001 pc and 0.09 pc away from the central flare, which are among the smallest ever reported for the proximity of dust to an SMBH. However, the anomalous *i*-band excess never seen in another TDE may be due to another reddening effect such as ERE.

We have shown the potential of TDEs to probe a new regime of dust around galaxy centers. These results are independent of the disputed TDE emission source and hence pose a robust use of TDEs. NIR observations are often excluded from high-cadence rapid follow up of TDEs in favor of early time X-ray and UV observations to constrain the flaring mechanism. However, the inclusion of the *i* band may not only probe different dust grain types and sizes than previously assumed for galactic nuclei, but in general, any IR observations achieved concurrent with the optical peak and decline may illuminate the closest surviving dust to SMBHs. We encourage systematic analysis of multiband optical light curves of TDEs with the inclusion of the *i* band or comparable NIR bands in high-cadence light curves, such as with ZTF samples, to explore the evidence of dust echoes in other sources, especially in cases with WISE light curves which indicate a dust echo as well. We similarly encourage follow up of ongoing and new interesting nuclear transients with NIR photometry in high-cadence optical surveys to probe a new regime of dust echo signatures.

Acknowledgments

M.N. is supported by the NSF Graduate Research Fellowship Program. D.A.H., E.P.G., and C.P. are supported by NSF grant Nos. AST-1911225 and AST-1911151. I.A. is a CIFAR Azrieli Global Scholar in the Gravity and the Extreme Universe Program and acknowledges support from that program, from the European Research Council (ERC) under the European Unions Horizon 2020 research and innovation program (grant No. 852097), from the Israel Science Foundation (grant No. 2752/19), from the United States Israel Binational Science Foundation (BSF), and from the Israeli Council for Higher Education Alon Fellowship. This research makes use of observations from the Las Cumbres Observatory global telescope network as well as the NASA/IPAC Extragalactic Database (NED), which is operated by the Jet Propulsion Laboratory, California Institute of Technology, under contract with NASA.

Facilities: LCOGT, Swift (XRT and UVOT), and WISE.

Software: astropy (Astropy Collaboration et al. 2013, 2018) and lcogtsnpipe (Valenti et al. 2016).

Appendix A
Filter Differences between ZTF and Las Cumbres

Although ZTF and the Las Cumbres Observatory both use filters described as *g* and *r* bands which are often analyzed simultaneously in transient reports, we find a significant difference between the ZTF and Las Cumbres *r*-band filters that warrants their individual analysis. In Figure 18 we show the synthetic photometry of 12 test spectra, each taken from Las Cumbres Observatory's 2 m telescope. We find that the ZTF *g*-band magnitudes derived from spectra are systematically dimmer than those of Las Cumbres' *g* band by an average 0.1 mag; by contrast, the ZTF *r* band derives synthetic photometry that is an average of 0.25 mag brighter than that of the Las Cumbres *r*-band filter. These differences, shown in Figure 18, produce light curves that may appear to have a wide scatter in *r*-band observations when the sensitivity curves of each filter are not properly taken into account, simultaneously affecting estimates in blackbody fitting and light-curve fitting with tools such as `MOSFiT` (Guillochon et al. 2018).

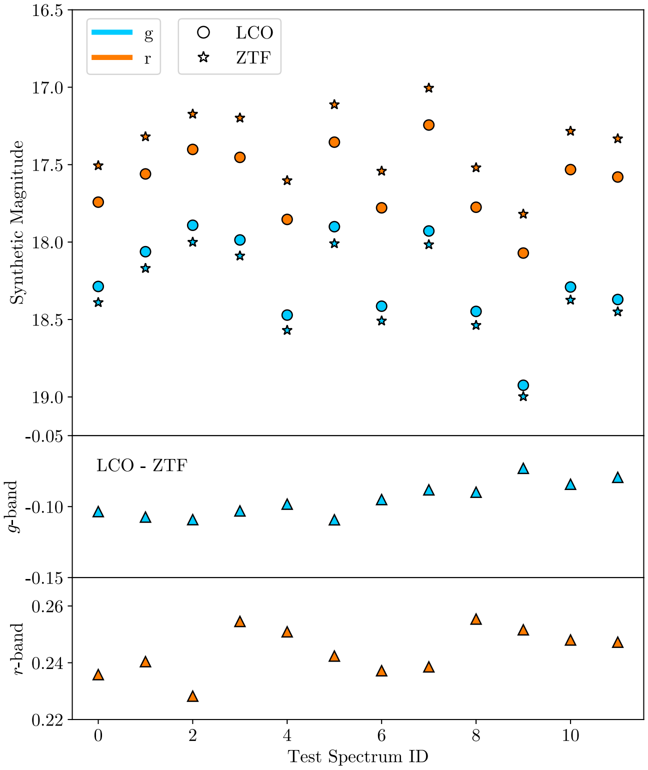

Figure 18. The synthetic photometry of 12 test spectra from FLOYDS-FTN when using Las Cumbres filters (filled circles) and ZTF filters (filled stars). The top panel shows both *g* (blue) and *r* photometry, the middle panel shows the difference between the magnitudes measured by LCO and ZTF in the *g* band, and the bottom panel shows that of the *r* band. The ZTF *r*-band synthetic photometry is an average of 0.25 mag brighter than that of the Las Cumbres *r*-band filter.

Appendix B
All Reduced Photometry

We report all photometry that was reduced and subtracted for this work from Las Cumbres in Table 4 and from Swift in Table 5. We also list the host galaxy photometry from both archival sources and Las Cumbres template images in Table 6.

B.1. Blackbody Fitting

We display corner plots of the blackbody fits to radius and temperature from the eight epochs with five or more filters of subtracted data within a 2 day range in Figure 19.

B.2. SMBH Mass Fits

We display the corner plot and light curve of AT 2020mot as fitted by MOSFiT in Figure 20 and the solutions for the black hole mass and stellar progenitor mass from TDEMass in Figure 21.

B.3. Host Photometry Analysis

`BAGPIPES` (Carnall et al. 2018) generates model spectra and fits to observed photometry of a galaxy to calculate the probability distribution functions (PDFs) of values relevant to the star formation history (SFH), dust, and metallicity. We start with the same choice of SFH and priors as in Carnall et al. (2018) for our initial fit. We use the stellar synthesis models as outlined in Bruzual & Charlot (2003) and updated in 2016[20]

---

[20] http://www.bruzual.org/~gbruzual/bc03/Updated_version_2016/

Table 4
Optical Photometry from the Las Cumbres Observatory, Reduced and Subtracted with `lcogtsnpipe`

MJD	*B*	*g*	*V*	*r*	*i*
59,078.6	18.30 ± 0.01	18.21 ± 0.03	18.25 ± 0.01	⋯	⋯
59,084.5	...	18.32 ± 0.02	⋯	18.50 ± 0.03	18.35 ± 0.05
59,089.5	18.47 ± 0.02	18.30 ± 0.01	18.35 ± 0.02	18.49 ± 0.02	18.36 ± 0.03
59,099.4	18.62 ± 0.02	⋯	18.57 ± 0.02	18.55 ± 0.03	18.33 ± 0.03
59,108.4	18.65 ± 0.02	18.57 ± 0.02	18.61 ± 0.03	18.75 ± 0.03	18.45 ± 0.04
59,113.2	18.73 ± 0.03	18.66 ± 0.02	18.56 ± 0.02	18.72 ± 0.03	18.56 ± 0.05
59,121.4	18.90 ± 0.03	18.79 ± 0.03	18.63 ± 0.03	18.92 ± 0.04	18.67 ± 0.05
59,128.4	18.99 ± 0.02	18.67 ± 0.03	18.91 ± 0.03	19.02 ± 0.05	18.68 ± 0.05
59,140.4	19.19 ± 0.03	19.08 ± 0.02	19.09 ± 0.04	19.16 ± 0.04	18.95 ± 0.05
59,145.2	19.32 ± 0.03	19.07 ± 0.02	19.25 ± 0.03	19.26 ± 0.04	18.94 ± 0.04
59,155.3	19.64 ± 0.09	⋯	19.36 ± 0.06	⋯	⋯
59,160.2	19.63 ± 0.04	19.38 ± 0.02	19.44 ± 0.06	19.43 ± 0.05	19.06 ± 0.05
59,165.3	19.78 ± 0.04	19.48 ± 0.03	19.61 ± 0.06	19.51 ± 0.04	19.04 ± 0.04
59,173.2	19.91 ± 0.05	19.48 ± 0.03	19.79 ± 0.04	19.57 ± 0.05	19.02 ± 0.04
59,178.3	20.07 ± 0.07	19.62 ± 0.05	19.76 ± 0.06	19.64 ± 0.10	⋯
59,202.2	⋯	19.82 ± 0.05	19.99 ± 0.09	19.70 ± 0.09	19.35 ± 0.08
59,222.2	⋯	20.13 ± 0.05	⋯	⋯	⋯
59,227.2	⋯	20.36 ± 0.08	⋯	⋯	19.54 ± 0.09
59,460.2	⋯	<22.28	⋯	<20.96	⋯
59,515.9	⋯	<22.37	⋯	<21.40	⋯
59,558.8	⋯	<22.10	⋯	⋯	19.95 ± 0.09

Note. *BV* magnitudes are given in the Vega system while *gri* magnitudes are given in the AB system.

Table 5
Ultraviolet Photometry from Swift-UVOT, Reduced and Subtracted with the `heasarc` Pipeline

MJD	*UVW2*	*UVW1*	*UVM2*	*U*
59,075.1	16.74 ± 0.03	16.80 ± 0.03	16.91 ± 0.03	17.19 ± 0.04
59,078.7	16.79 ± 0.10	16.79 ± 0.11	16.91 ± 0.11	17.22 ± 0.13
59,082.6	16.83 ± 0.09	0.00 ± 0.00	16.95 ± 0.09	17.30 ± 0.11
59,089.8	16.84 ± 0.09	16.95 ± 0.10	17.04 ± 0.10	17.50 ± 0.12
59,096.1	16.94 ± 0.10	17.14 ± 0.09	17.10 ± 0.09	17.57 ± 0.12
59,103.6	17.14 ± 0.10	17.07 ± 0.09	17.35 ± 0.10	0.00 ± 0.00
59,123.6	17.52 ± 0.10	17.41 ± 0.11	17.48 ± 0.11	17.75 ± 0.13
59,130.3	17.53 ± 0.10	17.67 ± 0.11	17.67 ± 0.11	17.97 ± 0.14
59,143.6	17.80 ± 0.07	18.04 ± 0.10	18.03 ± 0.10	0.00 ± 0.00
59,151.5	18.08 ± 0.12	0.00 ± 0.00	0.00 ± 0.00	0.00 ± 0.00

Note. Magnitudes are given in the Vega system.

Table 6
Photometry of the Host Galaxy WISEA J003113.52+850031.8 Used in Fitting with `BAGPIPES`

Filter	Source	Magnitude	Flux (μJy)
UVW2	Swift	20.19	6.88
UVM2	Swift	19.83	9.57
UVW1	Swift	19.55	15.66
B	Las Cumbres	18.84	119.705
g	PAN-STARRS	18.46	154.51
V	Las Cumbres	17.90	243.215
r	PAN-STARRS	17.73	300.47
i	PAN-STARRS	17.34	435.60
J	2MASS	15.54	966.0
H	2MASS	14.37	1180.0
K	2MASS	14.47	1090.0
W1	WISE	13.93	826.0
W2	WISE	13.89	429.0

Note. All magnitudes are given in the Vega system except for the *gri* magnitudes, which are given in the AB system.

assuming a Chabrier (2003) initial mass function. The SFH is modeled as a double power law,

$$\mathrm{SFR}(t) \propto \left[\left(\frac{t}{\tau}\right)^{\alpha}\left(\frac{t}{\tau}\right)^{-\beta}\right]^{-1}, \tag{B1}$$

where α and β are the rising and falling slopes, respectively, while τ is related to the time of peak star formation. Our priors on α and β are logarithmically uniform and range from 0.01 to 1000.0. We fit for metallicity with a uniform prior between 0.0 and 2.5 times solar metallicity, and we use a Calzetti et al. (2000) dust law with a uniform prior for extinction running from $A_V = (0.0, 4.0)$. We exclude a nebular component as the host spectrum does not show emission features. We also fix the redshift to the spectroscopically determined value $z = 0.07$. The SED fit is shown in Figure 22 and the resulting best-fit SFH is shown in Figure 23.

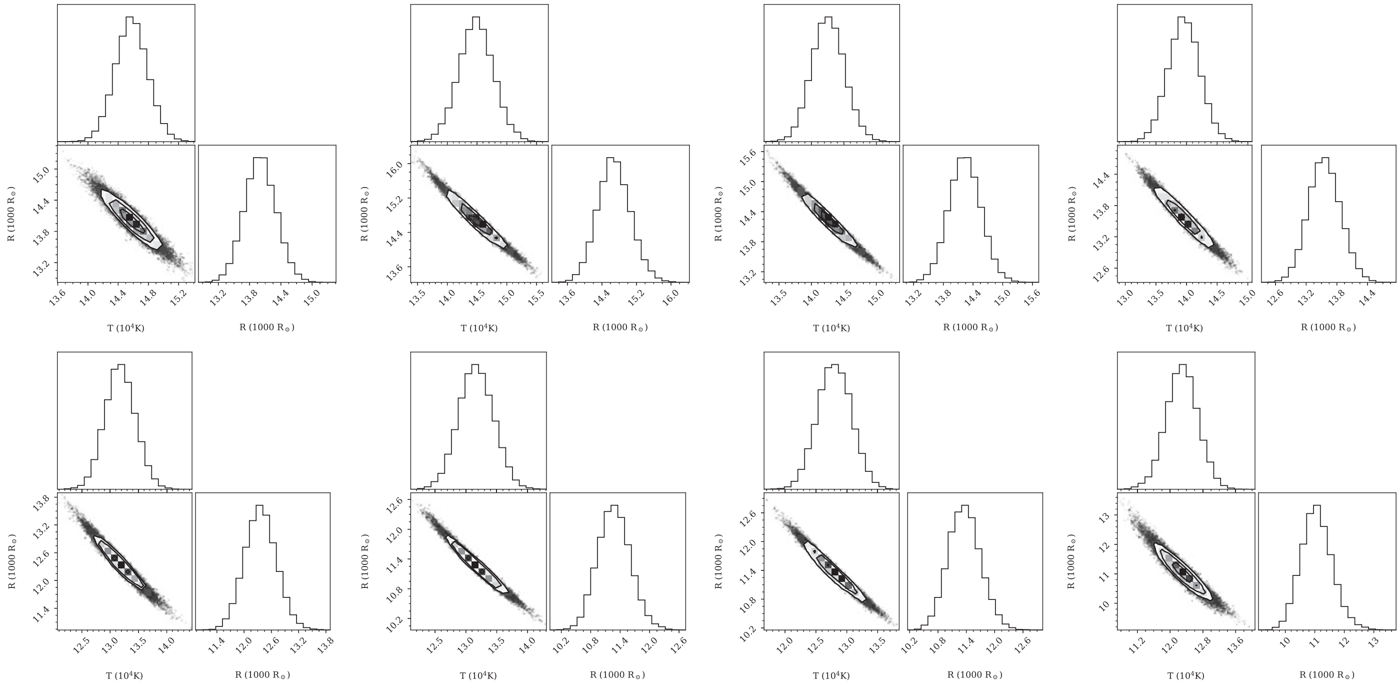

Figure 19. Corner plots of the light-curve fit to a blackbody temperature (*y*-axis, in 10^4 *K*) and radius (*x*-axis, in 1000 $R_\odot$) to each epoch with five filters of data available within a four day range. Top, left to right: MJD = 59,074.4, MJD = 59,078.102, MJD = 59,089.47, and MJD = 59,097.68; bottom, left to right: MJD = 59,129.58, MJD = 59,131.31, MJD = 59,144.80, and MJD = 59,152.87.

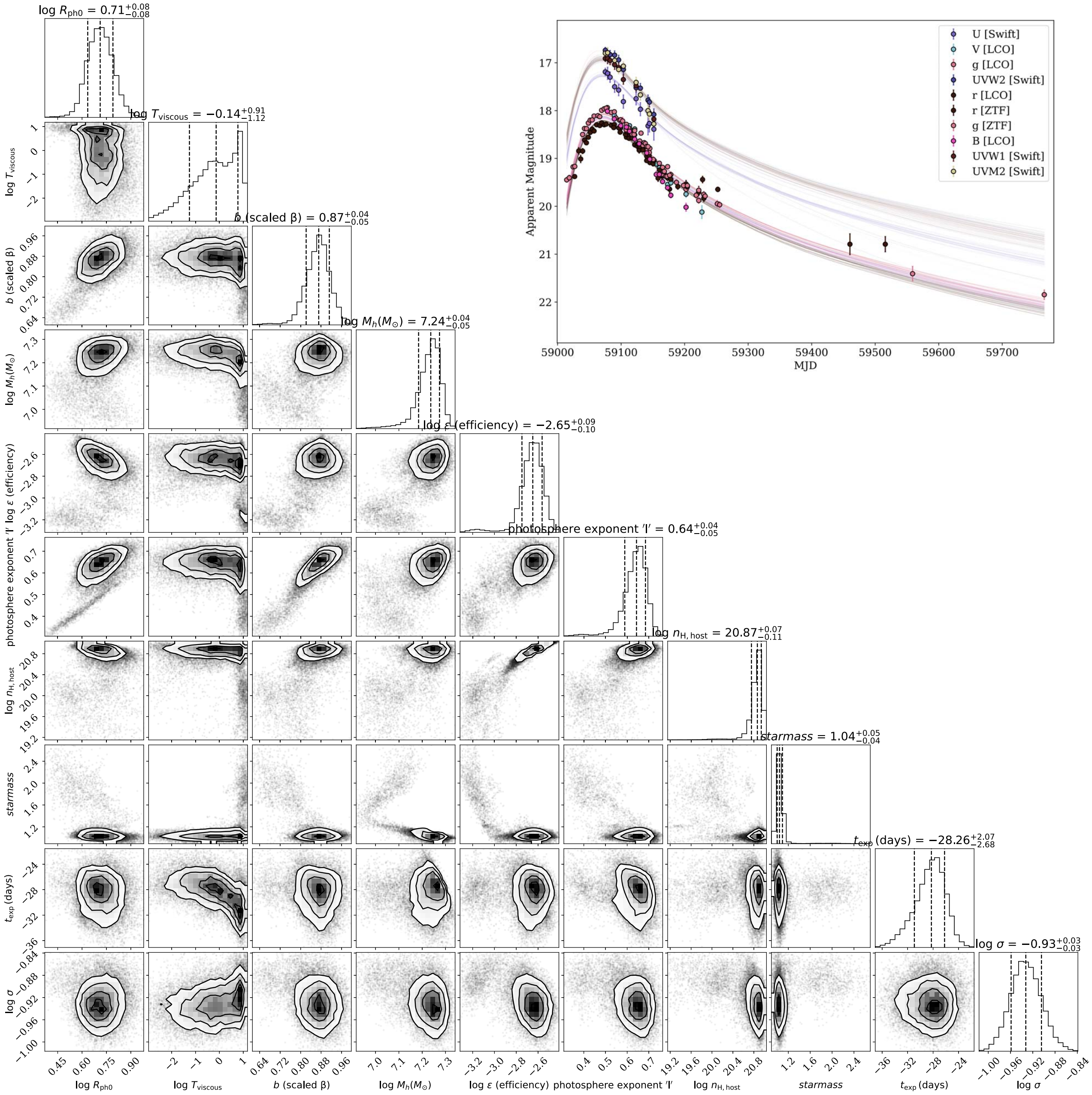

Figure 20. Corner plot and posterior light curves (upper right hand inset) from MOSFiT showing the convergence of parameter estimates based on fits to the UV/optical light curve of AT 2020mot.

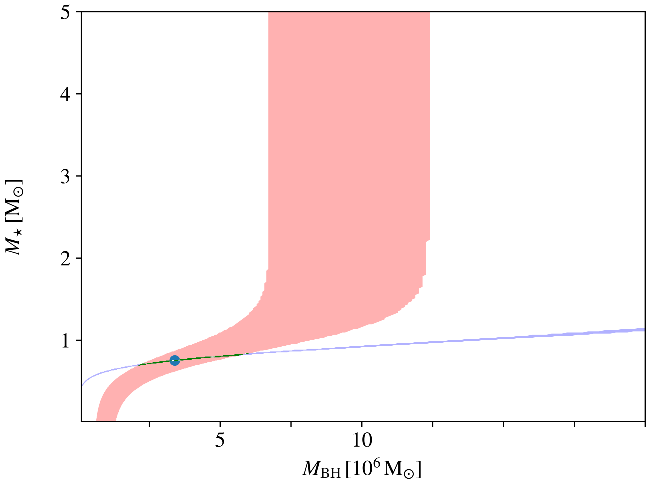

Figure 21. The output SMBH mass and star mass from TDEMass shown alongside their degeneracies. The blue line shows the solutions for masses from the given peak luminosity and the red strip shows the solutions from the peak temperature. The X-hatched green region thus indicates the overlapping solutions.

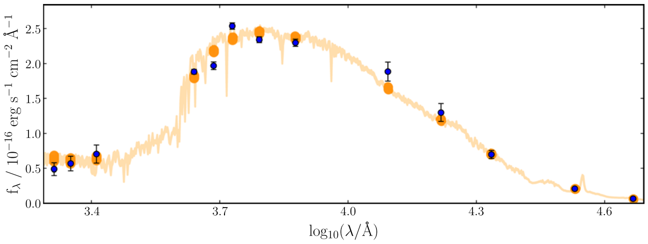

Figure 22. `BAGPIPES` fit to the WISEA J003113.52+850031.8 SED.

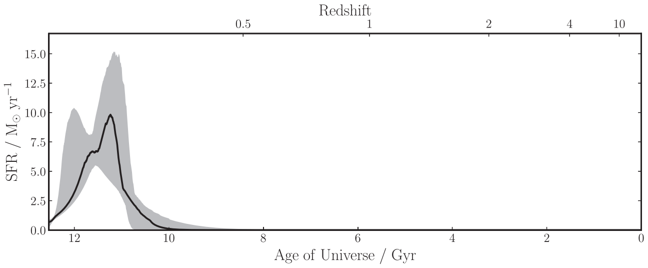

Figure 23. `BAGPIPES` best-fit SFH to the WISEA J003113.52+850031.8 SED.

ORCID iDs

Megan Newsome https://orcid.org/0000-0001-9570-0584
Iair Arcavi https://orcid.org/0000-0001-7090-4898
D. Andrew Howell https://orcid.org/0000-0003-4253-656X
Jamison Burke https://orcid.org/0000-0003-0035-6659
Kishalay De https://orcid.org/0000-0002-8989-0542
Yael Dgany https://orcid.org/0000-0002-7579-1105
Sara Faris https://orcid.org/0009-0007-8485-1281
Joseph Farah https://orcid.org/0000-0003-4914-5625
Daichi Hiramatsu https://orcid.org/0000-0002-1125-9187
Curtis McCully https://orcid.org/0000-0001-5807-7893
Estefania Padilla-Gonzalez https://orcid.org/0000-0003-0209-9246
Craig Pellegrino https://orcid.org/0000-0002-7472-1279
Giacomo Terreran https://orcid.org/0000-0003-0794-5982

References

Alard, C., & Lupton, R. H. 1998, ApJ, 503, 325
Arcavi, I. 2022, ApJ, 937, 75
Arcavi, I., Gal-Yam, A., Sullivan, M., et al. 2014, ApJ, 793, 38
Astropy Collaboration, Price-Whelan, A. M., Sipőcz, B. M., et al. 2018, AJ, 156, 123
Astropy Collaboration, Robitaille, T. P., Tollerud, E. J., et al. 2013, A&A, 558, A33
Barvainis, R. 1987, ApJ, 320, 537
Becker, A., 2015 HOTPANTS: High Order Transform of PSF ANd Template Subtraction, Astrophysics Source Code Library, ascl:1504.004
Bellm, E. C., Kulkarni, S. R., Graham, M. J., et al. 2019, PASP, 131, 018002
Blagorodnova, N., Gezari, S., Hung, T., et al. 2017, ApJ, 844, 46
Breeveld, A. A., Landsman, W., Holland, S. T., et al. 2011, in AIP Conf. Ser. 1358, Gamma Ray Bursts 2010, ed. J. E. McEnery, J. L. Racusin, & N. Gehrels (Melville, NY: AIP), 373
Brown, P. J., Breeveld, A. A., Holland, S., Kuin, P., & Pritchard, T. 2014, Ap&SS, 354, 89
Bruzual, G., & Charlot, S. 2003, MNRAS, 344, 1000
Calzetti, D., Armus, L., Bohlin, R. C., et al. 2000, ApJ, 533, 682
Carnall, A. C., McLure, R. J., Dunlop, J. S., & Davé, R. 2018, MNRAS, 480, 4379
Chabrier, G. 2003, PASP, 115, 763
Chang, H. C., Chen, K., & Kwok, S. 2006, ApJL, 639, L63
Chornock, R., Berger, E., Gezari, S., et al. 2014, ApJ, 780, 44
De, K., Hankins, M. J., Kasliwal, M. M., et al. 2020, PASP, 132, 025001
Dou, L., Wang, T. g., Jiang, N., et al. 2016, ApJ, 832, 188
Draine, B. T., & Lee, H. M. 1984, ApJ, 285, 89
Dwek, E. 1983, ApJ, 274, 175
Evans, C. R., & Kochanek, C. S. 1989, ApJL, 346, L13
Foreman-Mackey, D., Hogg, D. W., Lang, D., & Goodman, J. 2013, PASP, 125, 306
Forster, F., Bauer, F. E., Galbany, L., et al. 2020, TNSTR, 2020-1
French, K. D., Arcavi, I., & Zabludoff, A. 2016, ApJL, 818, L21
Gehrels, N., Chincarini, G., Giommi, P., et al. 2004, ApJ, 611, 1005
Gezari, S., Chornock, R., Lawrence, A., et al. 2015, ApJL, 815, L5
Gezari, S., Chornock, R., Rest, A., et al. 2012, Natur, 485, 217
Ghez, A. M., Hornstein, S. D., Lu, J. R., et al. 2005, ApJ, 635, 1087
Gomez, S., Nicholl, M., Short, P., et al. 2020, MNRAS, 497, 1925
Graham, M. J., Kulkarni, S. R., Bellm, E. C., et al. 2019, PASP, 131, 078001
Guillochon, J., Manukian, H., & Ramirez-Ruiz, E. 2014, ApJ, 783, 23
Guillochon, J., Nicholl, M., Villar, V. A., et al. 2018, ApJS, 236, 6
Hammerstein, E., van Velzen, S., Gezari, S., et al. 2023, ApJ, 942, 9
Henden, A. A., Welch, D. L., Terrell, D., & Levine, S. E. 2009, AAS, 214, 407.02
Hosseinzadeh, G., & Gomez, S., 2022 Light Curve Fitting v0.6.0, Zenododoi:10.5281/zenodo.6519623
Hosseinzadeh, G., Hiramatsu, D., DeMarchi, L., et al. 2020, TNSTR, 2020-2478
Hung, T., Gezari, S., Blagorodnova, N., et al. 2017, ApJ, 842, 29
Jiang, N., Dou, L., Wang, T., et al. 2016a, ApJL, 828, L14
Jiang, N., Wang, T., Hu, X., et al. 2021, ApJ, 911, 31
Jiang, N., Wang, T., Mou, G., et al. 2019, ApJ, 871, 15
Jiang, N., Wang, T., Yan, L., et al. 2017, ApJ, 850, 63
Jiang, Y. F., Guillochon, J., & Loeb, A. 2016b, ApJ, 830, 125
Kaiser, N., Burgett, W., Chambers, K., et al. 2010, Proc. SPIE, 7733, 77330E
Komossa, S., & Bade, N. 1999, A&A, 343, 775
Kormendy, J., & Ho, L. C. 2013, ARA&A, 51, 511
Kormendy, J., & Kennicutt, R. C. J. 2004, ARA&A, 42, 603
Koshida, S., Minezaki, T., Yoshii, Y., et al. 2014, ApJ, 788, 159
Lang, D. 2014, AJ, 147, 108
Li, D., Saxton, R. D., Yuan, W., et al. 2020, ApJ, 891, 121
Liodakis, I., Koljonen, K. I. I., Blinov, D., et al. 2023, Sci, 380, 656
Mainzer, A., Bauer, J., Cutri, R. M., et al. 2014, ApJ, 792, 30
Mainzer, A., Bauer, J., Grav, T., et al. 2011, ApJ, 731, 53
Masci, F. J., Laher, R. R., Rusholme, B., et al. 2019, PASP, 131, 018003
Meisner, A. M., Lang, D., & Schlegel, D. J. 2018, AJ, 156, 69
Minezaki, T., Yoshii, Y., Kobayashi, Y., et al. 2019, ApJ, 886, 150
Mockler, B., Guillochon, J., & Ramirez-Ruiz, E. 2019, ApJ, 872, 151
Munari, U., & Zwitter, T. 1997, A&A, 318, 269
Nicholl, M., Blanchard, P. K., Berger, E., et al. 2019, MNRAS, 488, 1878
Nicholl, M., Lanning, D., Ramsden, P., et al. 2022, MNRAS, 515, 5604
Onori, F., Cannizzaro, G., Jonker, P. G., et al. 2022, MNRAS, 517, 76
Patat, F. 2005, MNRAS, 357, 1161
Pierini, D., Majeed, A., Boroson, T. A., & Witt, A. N. 2002, ApJ, 569, 184

Piran, T., Svirski, G., Krolik, J., Cheng, R. M., & Shiokawa, H. 2015, ApJ, 806, 164
Poznanski, D., Prochaska, J. X., & Bloom, J. S. 2012, MNRAS, 426, 1465
Ramsden, P., Lanning, D., Nicholl, M., & McGee, S. L. 2022, MNRAS, 515, 1146
Rees, M. J. 1988, Natur, 333, 523
Rhee, Y. M., Lee, T. J., Gudipati, M. S., Allamandola, L. J., & Head-Gordon, M. 2007, PNAS, 104, 5274
Roming, P. W. A., Kennedy, T. E., Mason, K. O., et al. 2005, SSRv, 120, 95
Roth, N., Kasen, D., Guillochon, J., & Ramirez-Ruiz, E. 2016, ApJ, 827, 3
Ryu, T., Krolik, J., & Piran, T. 2020, ApJ, 904, 73
Schlafly, E. F., & Finkbeiner, D. P. 2011, ApJ, 737, 103
Sivan, J. P., & Perrin, J. M. 1993, ApJ, 404, 258
Skrutskie, M. F., Cutri, R. M., Stiening, R., et al. 2006, AJ, 131, 1163
Smith, T. L., & Witt, A. N. 2002, ApJ, 565, 304
Stein, R., Velzen, S. v., Kowalski, M., et al. 2021, NatAs, 5, 510
Szomoru, A., & Guhathakurta, P. 1998, ApJL, 494, L93
Valenti, S., Howell, D. A., Stritzinger, M. D., et al. 2016, MNRAS, 459, 3939
Valenti, S., Sand, D., Pastorello, A., et al. 2014, MNRAS, 438, L101
van Velzen, S., Gezari, S., Hammerstein, E., et al. 2021b, ApJ, 908, 4
van Velzen, S., Mendez, A. J., Krolik, J. H., & Gorjian, V. 2016, ApJ, 829, 19
van Velzen, S., Pasham, D. R., Komossa, S., Yan, L., & Kara, E. A. 2021a, SSRv, 217, 63
Wang, Y., Jiang, N., Wang, T., et al. 2022, ApJL, 930, L4
Wevers, T., Gromadzki, M., Lyman, J., & Yaron, O. 2018, TNSTR, 2018-1397
Wevers, T., Pasham, D. R., van Velzen, S., et al. 2019, MNRAS, 488, 4816
Wright, E. L., Eisenhardt, P. R. M., Mainzer, A. K., et al. 2010, AJ, 140, 1868
Yao, Y., Ravi, V., Gezari, S., et al. 2023, ApJL, 955, L6
Zabludoff, A. I., Zaritsky, D., Lin, H., et al. 1996, ApJ, 466, 104
Zackay, B., Ofek, E. O., & Gal-Yam, A. 2016, ApJ, 830, 27